J. Fluid Mech. (2020), *vol.* 891, A23. © The Author(s), 2020.
Published by Cambridge University Press
doi:10.1017/jfm.2020.153

Large-amplitude membrane flutter in inviscid flow

C. Mavroyiakoumou[1,†] **and S. Alben**[1,†]

[1]Department of Mathematics, University of Michigan, Ann Arbor, MI 48109, USA

(Received 29 July 2019; revised 18 December 2019; accepted 19 February 2020)

We study the large-amplitude flutter of membranes (of zero bending rigidity) with vortex sheet wakes in two-dimensional inviscid fluid flows. We apply small initial deflections and track their exponential decay or growth and subsequent large-amplitude dynamics in the space of three dimensionless parameters: membrane pretension, mass density and stretching modulus. With both ends fixed, all the membranes converge to steady deflected shapes with single humps that are nearly fore-aft symmetric, except when the deformations are unrealistically large. With leading edges fixed and trailing edges free to move in the transverse direction, the membranes flutter periodically at intermediate values of mass density. As mass density increases, the motions are increasingly aperiodic, and the amplitudes increase and spatial and temporal frequencies decrease. As mass density decreases from the periodic regime, the amplitudes decrease and spatial and temporal frequencies increase until the motions become difficult to resolve numerically. With both edges free to move in the transverse direction, the membranes flutter similarly to the fixed–free case, but also translate vertically with steady, periodic or aperiodic trajectories, and with non-zero slopes that lead to small angles of attack with respect to the oncoming flow.

Key words: flow–structure interactions, nonlinear instability, vortex shedding

1. Introduction

There is a wealth of literature describing the fluid dynamics induced by the motion of a flexible body through a fluid flow. In most studies the body motion is bending dominated, with a moderate bending modulus, but essentially inextensible (Taneda 1968; Kornecki, Dowell & O'Brien 1976; Zhang *et al.* 2000; Watanabe *et al.* 2002; Zhu & Peskin 2002; Argentina & Mahadevan 2005; Shelley, Vandenberghe & Zhang 2005; Eloy, Souilliez & Schouveiler 2007; Alben 2008*b*; Alben & Shelley 2008; Eloy *et al.* 2008; Michelin, Smith & Glover 2008; Shelley & Zhang 2011). A smaller number of studies, including this one, consider softer materials – extensible membranes – that have a negligible bending modulus, and undergo significant stretching in a fluid flow (Newman & Paidoussis 1991; Lian & Shyy 2005; Sygulski 2007; Song *et al.* 2008; Tiomkin & Raveh 2017; Tzezana & Breuer 2019). Examples

† Email addresses for correspondence: chrismav@umich.edu, alben@umich.edu

https://doi.org/10.1017/jfm.2020.153 Published online by Cambridge University Press

are rubber, textile fabric or the skin of swimming and flying animals (Newman 1987; Lian *et al.* 2003; Lauder *et al.* 2006; Cheney *et al.* 2015).

Here we extend our model of an inextensible bending body with a vortex sheet wake (Alben 2008*a*, 2009) to an extensible membrane. Our previous work investigated the nonlinear dynamics of a periodically pitching flexible body in a fluid stream (Alben 2009) and the flapping-flag instability (Alben & Shelley 2008), among many other studies of this problem (Tang, Yamamoto & Dowell 2003; Shelley *et al.* 2005; Eloy *et al.* 2007; Michelin *et al.* 2008; Huang & Sung 2010; Chen *et al.* 2014; Alben 2015). As bending rigidity is decreased below the flutter threshold, the flag transitions from periodic to chaotic dynamics. Our model includes the separation of vortex sheets at sharp edges (Krasny 1991; Nitsche & Krasny 1994; Jones 2003; Jones & Shelley 2005), and regularizes free vortex sheets to avoid singularities (Chorin & Bernard 1973; Krasny 1986; Brady, Leonard & Pullin 1998; Nitsche, Taylor & Krasny 2003; Alben 2010).

In this model, vortex sheets approximate the thin viscous boundary layers along the body, which are advected from its trailing edge into the flow downstream. This can be regarded as the inviscid limit of the viscous flow, and gives a good representation of the large-scale features of the flow and the vortex wake dynamics at Reynolds numbers of $O(10^2–10^5)$ (Nitsche & Krasny 1994; Shukla & Eldredge 2007; Sheng *et al.* 2012; Xu, Nitsche & Krasny 2017). These flows are challenging to simulate directly due to the need to resolve sharp layers of vorticity in the vicinity of an unsteady, possibly deforming solid boundary. The immersed boundary method (Peskin 2002; Zhu & Peskin 2002; Griffith & Peskin 2005; Taira & Colonius 2007; Ghias, Mittal & Dong 2007; Tytell *et al.* 2010; Hamlet, Santhanakrishnan & Miller 2011; Tian *et al.* 2011) can successfully simulate this class of problems. Very fine grids are needed to resolve the vorticity, and these are refined adaptively for efficiency (Roma, Peskin & Berger 1999; Griffith *et al.* 2007). However, by only computing flow quantities on one-dimensional contours (the body and the vortex sheet wake), the vortex sheet model is typically much less expensive to compute when the far-field wake is approximated, as described in appendix B.

The focus of the present study is extensible membrane flutter: how a membrane initially aligned with a fluid flow becomes unstable to transverse deflections and eventually reaches steady-state large-amplitude dynamics. Large-amplitude membrane flutter can affect the performance of membrane aircraft (Lian & Shyy 2005; Hu, Tamai & Murphy 2008; Stanford *et al.* 2008; Jaworski & Gordnier 2012; Piquee *et al.* 2018; Schomberg *et al.* 2018; Tzezana & Breuer 2019), sails (Colgate 1996; Kimball 2009), pneumatic membrane structures such as hanging roofs (Haruo 1975; Knudson 1991; Sygulski 1996, 1997, 2007), and can occur in the human palate, resulting in snoring (Ellis, Williams & Shneerson 1993; Huang 1995*a*,*b*; Wang, Rebeiz & Shapshay 2002; Howell *et al.* 2009). The initial small-amplitude stage of the flutter instability has been the focus of several experimental, theoretical and numerical studies, summarized in table 1. We classify these and the present study in terms of three dimensionless parameters: membrane mass density, stretching modulus and pretension. The present simulations allow us to consider wide ranges of the parameters including those of the previous studies. Newman & Paidoussis (1991) used an infinite periodic membrane model with a low-mode approximation and found that stability is lost through divergence. Le Maître, Huberson & De Cursi (1999) used a vortex sheet model to study a more complex situation – the motions of a sail membrane under harmonic perturbations of the trailing edge and with randomly perturbed inflow velocities. Sygulski (2007) studied the membrane flutter threshold

https://doi.org/10.1017/jfm.2020.153 Published online by Cambridge University Press

Study	$R_1 = \dfrac{\rho_s h}{\rho_f L}$	$R_3 = \dfrac{Eh}{\rho_f U^2 L}$	$T_0 = \dfrac{\overline{T}}{\rho_f U^2 L W}$
Newman & Paidoussis (1991)^t	0–6	—	0–2
Le Maître *et al.* (1999)^e	0–0.8	10, 50, 100, 500, 1000	—
Sygulski (2007)$^{e\,\text{and}\,t}$	0.1, 1	—	130.6, 217
Jaworski & Gordnier (2012)$^{c\,\text{and}\,e}$	1.2	100, 200, 400, 614	4, 10, 20, 30.7
Tiomkin & Raveh (2017)^c	0–80	—	0–6
Nardini *et al.* (2018)^c	0–60	—	0–3
Present study$^{c\,\text{and}\,t}$	0.001–100	1–10 000	0.001–1000

TABLE 1. Summary of parameter ranges used in previous and current membrane studies. Computational (^{c}), experimental (^{e}) or theoretical (^{t}) ranges of the dimensionless body mass density R_1, stretching modulus R_3 and pretension T_0, defined in § 2.1.

and divergence modes theoretically, with some experimental validation. Tiomkin & Raveh (2017) presented a more detailed flutter threshold calculation using an inviscid, small amplitude vortex sheet model. Nardini, Illingworth & Sandberg (2018) compared a reduced-order model with direct numerical simulations to study the effect of Reynolds number on the flutter stability threshold and small-amplitude membrane deflection modes. So far there has been relatively little work on the large-amplitude dynamics following the initial flutter instability, and this is the focus of the present work.

Another main topic of fluid-membrane interaction studies is bio-inspired propulsion. Piquee *et al.* (2018) studied how a membrane wing adjusts its shape to fluid pressure loading at various angles of attack. Tzezana & Breuer (2019) coupled thin airfoil theory with a membrane equation to study the effects of wing compliance, inertia and flapping kinematics on aerodynamic performance. Jaworski & Gordnier (2012) studied a heaving and pitching membrane airfoil in a fluid stream numerically at Reynolds number 2500, and found elastic modulus and prestress parameters that led to enhanced thrust and propulsive efficiency. The passive adaptivity of a membrane wing has the potential to increase lift forces and delay the occurrence of stall to higher angles of attack for micro-air vehicles (MAVs) (Lian & Shyy 2005; Hu *et al.* 2008; Stanford *et al.* 2008). Schomberg *et al.* (2018) used electrostatic forces to control a membrane shape and delay the transition from a laminar boundary layer, reducing viscous drag. Here, however, we focus solely on the flutter problem and defer propulsion-related dynamics to future work.

2. Membrane-vortex-sheet model

We first consider the motion of an extensible membrane that is fixed at two endpoints and held in a two-dimensional fluid flow, like much of the previous work. A uniform background flow is prescribed with velocity U, directed parallel to the chord connecting the endpoints (see figure 1). The instantaneous position of the membrane is given by $\boldsymbol{X}(\alpha, t) = (x(\alpha, t), y(\alpha, t))$, parameterized by the material coordinate α, $-L \leqslant \alpha \leqslant L$ (L is half the chord length) and time t. It is convenient to also describe the membrane position in complex notation, $\zeta(\alpha, t) = x(\alpha, t) + \mathrm{i}y(\alpha, t)$. The inviscid flow can be represented by a vortex sheet – a curve across which the tangential velocity component is discontinuous (Saffman 1992) – and whose position and strength evolve in time. The vortex sheet consists of two parts. One is 'bound'

https://doi.org/10.1017/jfm.2020.153 Published online by Cambridge University Press

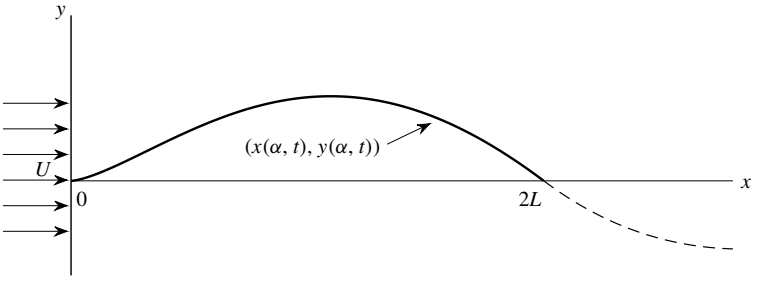


FIGURE 1. Schematic diagram of a flexible membrane (solid curved line) at an instant in time. Here $2L$ is the chord length (the distance between the endpoints), U is the oncoming flow velocity, $(x(\alpha, t), y(\alpha, t))$ is the membrane position and the dashed line is the free vortex sheet wake.

(it coincides with the membrane, for $-L \leqslant \alpha \leqslant L$), and the other is 'free,' emanating from the trailing edge of the membrane at $\alpha = L$. The bound and free vortex sheets have strength densities denoted by γ and positions denoted by ζ.

The membrane dynamics are described by the unsteady extensible elastica equation with body inertia, stretching resistance and fluid pressure loading (Tadjbakhsh 1966), obtained by writing a force balance equation for a small section of membrane lying between α and $\alpha + \Delta\alpha$:

$$\rho_s h W \partial_{tt} \zeta(\alpha, t) \Delta\alpha = T(\alpha + \Delta\alpha, t)\hat{\boldsymbol{s}} - T(\alpha, t)\hat{\boldsymbol{s}} - [p](\alpha, t)\hat{\boldsymbol{n}} W(s(\alpha + \Delta\alpha, t) - s(\alpha, t)). \tag{2.1}$$

Dividing by $\Delta\alpha$ and taking the limit $\Delta\alpha \to 0$, we obtain

$$\rho_s h W \partial_{tt} \zeta(\alpha, t) = \partial_\alpha (T(\alpha, t)\hat{\boldsymbol{s}}) - [p](\alpha, t) W \partial_\alpha s \hat{\boldsymbol{n}}, \tag{2.2}$$

where ρ_s is the mass per unit volume of the undeflected membrane, h is its thickness and W is its out-of-plane width, all uniform along the length. The material coordinate $\alpha \in [-L, L]$ is the x-coordinate of the membrane in the initial flat, uniformly prestretched state. Other quantities that appear in (2.2) are $\hat{\boldsymbol{s}}, \hat{\boldsymbol{n}} \in \mathbb{C}$, which represent the unit vectors tangent and normal to the membrane, respectively,

$$\hat{\boldsymbol{s}} = \partial_\alpha \zeta(\alpha, t)/\partial_\alpha s(\alpha, t) = \mathrm{e}^{\mathrm{i}\theta(\alpha,t)} \quad \text{and} \quad \hat{\boldsymbol{n}} = \mathrm{i}\hat{\boldsymbol{s}} = \mathrm{i}\mathrm{e}^{\mathrm{i}\theta(\alpha,t)}, \tag{2.3a,b}$$

with $\theta(\alpha, t)$ the local tangent angle, $s(\alpha, t)$ the local arc length coordinate and $\kappa(\alpha, t) = \partial_\alpha \theta / \partial_\alpha s$ the membrane's curvature. Here $[p](\alpha, t)$ is the local pressure difference across the membrane, from the side toward which $\hat{\boldsymbol{n}}$ points to the other side.

The membrane tension $T(\alpha, t)$ is given by linear elasticity (Carrier 1945, 1949; Narasimha 1968; Nayfeh & Pai 2008), i.e.

$$T(\alpha, t) = \overline{T} + EhW(\partial_\alpha s(\alpha, t) - 1), \tag{2.4}$$

where E is the Young's modulus. Thus, the tension is a constant $\overline{T}$, the 'pretension,' in the (initial) undeflected equilibrium state $\zeta(\alpha, 0) = \alpha$.

https://doi.org/10.1017/jfm.2020.153 Published online by Cambridge University Press

2.1. *Non-dimensionalization*

We non-dimensionalize the governing equations by the density of the fluid ρ_f, the half-chord L and the imposed fluid flow velocity U. In particular, we use

$$\tilde{t} = \frac{t}{L/U}, \quad (\tilde{\zeta}, \tilde{\alpha}, \tilde{s}) = \frac{(\zeta, \alpha, s)}{L}, \quad \widetilde{[p]} = \frac{[p]}{\rho_f U^2}. \tag{2.5a–c}$$

The membrane equation (2.2) becomes

$$\frac{\rho_s h U^2 W}{L} \widetilde{\partial_{tt}\zeta} = \frac{1}{L} \widetilde{\partial}_\alpha [(\overline{T} + EhW(\widetilde{\partial_\alpha s} - 1))\hat{\boldsymbol{s}}] - \rho_f U^2 W \widetilde{[p]} \widetilde{\partial_\alpha s} \hat{\boldsymbol{n}}, \tag{2.6}$$

with dimensionless quantities (and their dimensionless derivatives) denoted by tildes. Dividing (2.6) by $\rho_f U^2 W$ throughout yields

$$\frac{\rho_s h}{\rho_f L} \widetilde{\partial_{tt}\zeta} = \frac{1}{\rho_f U^2 L W} \widetilde{\partial}_\alpha [(\overline{T} + EhW(\widetilde{\partial_\alpha s} - 1))\hat{\boldsymbol{s}}] - \widetilde{[p]} \widetilde{\partial_\alpha s} \hat{\boldsymbol{n}}. \tag{2.7}$$

Thus, the dimensionless membrane equation (dropping tildes) is

$$R_1 \partial_{tt}\zeta - \partial_\alpha ((T_0 + R_3(\partial_\alpha s - 1))\hat{\boldsymbol{s}}) = -[p]\partial_\alpha s \hat{\boldsymbol{n}}. \tag{2.8}$$

The dimensionless parameters of the membrane are

$$R_1 = \frac{\rho_s h}{\rho_f L}, \quad T_0 = \frac{\overline{T}}{\rho_f U^2 L W} \quad \text{and} \quad R_3 = \frac{Eh}{\rho_f U^2 L}, \tag{2.9a–c}$$

where R_1, T_0 and R_3 are the dimensionless membrane mass density, pretension and stretching modulus, respectively. We assume that the thickness ratio h/L is small, but ρ_s/ρ_f may be large, so R_1 may assume any non-negative value. We have neglected bending rigidity, denoted R_2 in Alben & Shelley (2008). In the extensible membrane regime studied here, R_3 is finite, so $R_2 = R_3 h^2/12L^2 \to 0$ in the limit $h/L \to 0$. By contrast, the inextensible beam or plate regime studied previously (Tang *et al.* 2003; Shelley *et al.* 2005; Eloy *et al.* 2007; Michelin *et al.* 2008; Huang & Sung 2010; Chen *et al.* 2014; Alben 2015) has R_2 finite and $R_3 \to +\infty$ as $(h/L)^{-2}$ in the limit $h/L \to 0$, resulting in inextensibility. We have also neglected the effects of rotary inertia and the Poisson ratio (the transverse contraction due to axial stretching), which have usually been neglected at leading order in nonlinear membrane models (Nayfeh & Pai 2008) and the aforementioned membrane studies. The rotary inertia and bending rigidity terms are given in Tadjbakhsh (1966), and those involving the Poisson ratio are given in Nayfeh & Pai (2008).

For large-Reynolds-number flows, there are thin viscous boundary layers along the sides of the membrane. Across these boundary layers, the component of fluid velocity that is tangent to the membrane is brought to zero on the membrane (Batchelor 1967). When the fluid in the boundary layer is advected off of the membrane's trailing edge, a free shear layer forms (Saffman 1992; Alben 2010). In the limit of large Reynolds number, the two boundary layers tend to vortex sheets which coincide as a single bound vortex sheet (approximating the body thickness as zero for the fluid computation). The free shear layer tends to a free vortex sheet (Saffman 1992).

https://doi.org/10.1017/jfm.2020.153 Published online by Cambridge University Press

The free sheet circulation is defined as an integral of the vortex sheet strength γ (the jump in the tangential component of the fluid velocity) over the free vortex sheet

$$\Gamma(s,t) = -\int_s^{s_{max}} \gamma(s',t)\,\mathrm{d}s', \quad 0 < s < s_{max}, \tag{2.10}$$

where s is the arc length along the free sheet, starting from 0 where the free sheet meets the membrane's trailing edge and ending at s_{max} at the free sheet's far end. Following Jones (2003) and Alben (2009), we define the (negative of the) total circulation in the free sheet as

$$\Gamma_+(t) = \Gamma(0,t) = -\int_0^{s_{max}} \gamma(s,t)\,\mathrm{d}s. \tag{2.11}$$

The complex conjugate of the flow velocity $\boldsymbol{u} = (u_x, u_y)$ at any point z in the flow (not on the vortex sheets) can be calculated in terms of γ by integrating the vorticity in the bound and free vortex sheets against the Biot–Savart kernel (Saffman 1992), i.e.

$$u_x(z) - \mathrm{i}u_y(z) = 1 + \frac{1}{2\pi\mathrm{i}}\int_{-1}^{1} \frac{\gamma(\alpha,t)}{z-\zeta(\alpha,t)}\partial_\alpha s(\alpha,t)\,\mathrm{d}\alpha + \frac{1}{2\pi\mathrm{i}}\int_0^{s_{max}} \frac{\gamma(s,t)}{z-\zeta(s,t)}\,\mathrm{d}s, \tag{2.12}$$

with unity on the right-hand side representing the imposed background flow and the dimensionless material coordinate α ranging from -1 to 1 on the membrane. By Kelvin's circulation theorem, Γ is conserved at fixed material elements of the free vortex sheet. Thus, we reparameterize the free sheet position as $\zeta(\Gamma,t)$ and evolve the position at a fixed Γ simply by following the local fluid velocity. This is done by taking the average of the limits of (2.12) as z approaches $\zeta(\Gamma,t)$ from both sides (Saffman 1992):

$$\frac{\partial\overline{\zeta}}{\partial t}(\Gamma,t) = 1 + \frac{1}{2\pi\mathrm{i}}\int_{-1}^{1} \frac{\gamma(\alpha,t)}{\zeta(\Gamma,t)-\zeta(\alpha,t)}\partial_\alpha s(\alpha,t)\,\mathrm{d}\alpha - \frac{1}{2\pi\mathrm{i}}\fint_0^{\Gamma_+(t)} \frac{\mathrm{d}\Gamma'}{\zeta(\Gamma,t)-\zeta(\Gamma',t)}. \tag{2.13}$$

In (2.13), $\partial\overline{\zeta}/\partial t$ is the complex conjugate velocity at $\zeta(\Gamma,t)$, and the second integral is a Cauchy-principal-value integral. We have reparameterized the free sheet integral using $\gamma\,\mathrm{d}s = -\mathrm{d}\Gamma$. This form of the integral appears in the Birkhoff–Rott equation for the evolution of a free vortex sheet (Saffman 1992; Jones 2003; Pullin & Wang 2004; Jones & Shelley 2005). In this form $\mathrm{d}\Gamma$ may have either sign.

We may solve for the bound vortex sheet strength $\gamma(\alpha,t)$ in terms of the membrane velocity by equating the components of the fluid and membrane velocities normal to the membrane ('the kinematic condition'), which are found by taking the average of the limits of (2.13) as z approaches the membrane from both sides:

$$\begin{aligned} &Re(\hat{\boldsymbol{n}}\partial_t\overline{\zeta}(\alpha,t)) \\ &\quad = Re\left(\hat{\boldsymbol{n}}\left(1 + \frac{1}{2\pi\mathrm{i}}\fint_{-1}^{1} \frac{\gamma(\alpha',t)\partial_\alpha s(\alpha',t)}{\zeta(\alpha,t)-\zeta(\alpha',t)}\,\mathrm{d}\alpha' - \frac{1}{2\pi\mathrm{i}}\int_0^{\Gamma_+(t)} \frac{\mathrm{d}\Gamma'}{\zeta(\alpha,t)-\zeta(\Gamma',t)}\right)\right). \end{aligned} \tag{2.14}$$

When the left-hand side and the second integral on the right-hand side of (2.14) are known, the general solution $\gamma(\alpha,t)$ has inverse-square-root singularities at $\alpha = \pm 1$. Therefore, we define $v(\alpha,t)$, the bounded part of $\gamma(\alpha,t)$, by

$$\gamma(\alpha,t) = \frac{v(\alpha,t)}{\sqrt{1-\alpha^2}}. \tag{2.15}$$

https://doi.org/10.1017/jfm.2020.153 Published online by Cambridge University Press

An additional scalar constraint is required to uniquely specify the solution γ (or v) to (2.14). It is the conservation of total circulation (Kelvin's circulation theorem):

$$\int_{-1}^{1} \gamma\, \partial_\alpha s \,\mathrm{d}\alpha = \int_{-1}^{1} \frac{v(\alpha, t)}{\sqrt{1-\alpha^2}} \partial_\alpha s \,\mathrm{d}\alpha = \Gamma_+(t). \tag{2.16}$$

In (2.13) and (2.14) it is helpful to replace the free sheet integral with a regularized version to avoid singularities in the sheet curvature (Krasny 1986). The second integral in (2.13) becomes

$$-\frac{1}{2\pi \mathrm{i}} \int_0^{\Gamma_+(t)} \frac{\overline{\zeta(\Gamma, t) - \zeta(\Gamma', t)}}{|\zeta(\Gamma, t) - \zeta(\Gamma', t)|^2 + \delta(\Gamma', t)^2} \,\mathrm{d}\Gamma', \tag{2.17}$$

with a regularization parameter

$$\delta(\Gamma, t) = \delta_0 (1 - \mathrm{e}^{-s(\Gamma,t)^2/\varepsilon^2}). \tag{2.18}$$

The effect of δ is to inhibit the growth of free sheet structures (e.g. inner turns of spirals) on scales smaller than δ while maintaining the shape and motion of the sheet on larger scales. Our choice of δ tends to 0 quadratically over a scale given by ε as the membrane trailing edge is approached, to decrease the effect of regularization on the flow near the trailing edge and the production of circulation (Alben 2009, 2010). Here we set ε to 0.4 and δ_0 to 0.2, choices that make the effect of regularization on circulation production small without a significant increase in the total number of points needed to resolve the free sheet (Alben 2010). The Kutta condition determines the rate of circulation production $\mathrm{d}\Gamma_+(t)/\mathrm{d}t$ by making the fluid velocity at the trailing edge finite. This means $\gamma(1, t)$ must be finite, and, thus, $v(1, t) = 0$ by (2.15).

The vortex sheet strength $\gamma(\alpha, t)$ is coupled to the pressure jump $[p](\alpha, t)$ across the membrane using a version of the unsteady Bernoulli equation written at a fixed material point on the membrane:

$$\partial_\alpha s \partial_t \gamma + (\mu - \tau)\partial_\alpha \gamma + \gamma(\partial_\alpha \mu - \partial_\alpha s \nu \kappa) = \partial_\alpha [p]. \tag{2.19}$$

This equation is derived in appendix A, and generalizes the derivation in Alben (2012, appendix A) to the case of an extensible body.

In (2.19), μ is the tangential component of the average flow velocity at the membrane,

$$\mu(\alpha, t) = Re\left(\hat{\boldsymbol{s}}\left(1 + \frac{1}{2\pi \mathrm{i}} \int_{-1}^{1} \frac{\gamma(\alpha', t)\partial_\alpha s(\alpha', t)}{\zeta(\alpha, t) - \zeta(\alpha', t)} \,\mathrm{d}\alpha' - \frac{1}{2\pi \mathrm{i}} \int_0^{\Gamma_+(t)} \frac{\mathrm{d}\Gamma'}{\zeta(\alpha, t) - \zeta(\Gamma', t)}\right)\right), \tag{2.20}$$

and τ and ν are respectively the components of the membrane's velocity tangent and normal to itself:

$$\tau(\alpha, t) = Re(\partial_t \overline{\zeta}(\alpha, t)\hat{\boldsymbol{s}}); \quad \nu(\alpha, t) = Re(\partial_t \overline{\zeta}(\alpha, t)\hat{\boldsymbol{n}}). \tag{2.21a,b}$$

The pressure jump across the free sheet is zero, which yields

$$[p]|_{\alpha=1} = 0, \tag{2.22}$$

the boundary condition we use to integrate (2.19) and obtain $[p](\alpha, t)$ on the membrane.

https://doi.org/10.1017/jfm.2020.153 Published online by Cambridge University Press

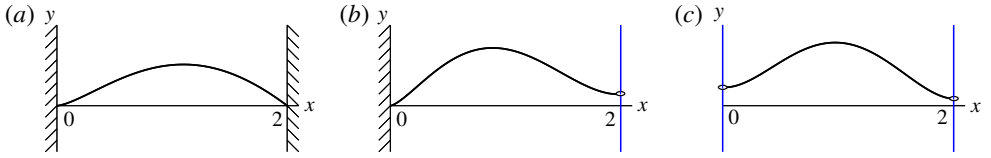


FIGURE 2. Schematic diagrams of the three sets of boundary conditions considered: fixed–fixed (*a*), fixed–free (*b*), and free–free (*c*).

2.2. *Boundary and initial conditions*

We investigate three cases of boundary conditions at the two ends of the membrane, shown schematically in figure 2. In all three cases, the x-coordinates of the ends are constant: $x(-1, t) = 0$ and $x(1, t) = 2$. In the first case, 'fixed–fixed,' the membrane is flat at $t = 0$, and we set the deflection to zero at both ends of the membrane after a small initial perturbation. More precisely, we smoothly perturb y at the leading edge slightly away from zero and relax it to zero exponentially in time, i.e.

$$y(-1, t) = \sigma \left(\frac{t}{\eta}\right)^3 \mathrm{e}^{-(t/\eta)^3}, \tag{2.23}$$

where σ is a constant chosen in the range 10^{-6}–10^{-3} (depending on whether small or large amplitude dynamics are studied) and $\eta = 0.2$. We set the trailing edge deflection $y(1, t)$ to zero for all t. This is essentially the case considered by most previous studies of membrane flutter (Le Maître *et al.* 1999; Sygulski 2007; Tiomkin & Raveh 2017; Nardini *et al.* 2018), and here we find, surprisingly, that all physically reasonable deflected membrane states are steady (i.e. without oscillations). In the second case, 'fixed–free,' we again make the membrane flat initially and then set the leading edge position according to (2.23), but allow the trailing edge to deflect freely in the vertical direction. This is the classical free-end boundary condition for a membrane (Graff 1975; Farlow 1993) and corresponds to the membrane end fixed to a massless ring that slides without friction along a vertical pole (see figure 2*b*). Without friction, the force from the pole on the ring at the membrane end is horizontal. The tension force from the membrane on the ring must also be horizontal, or else the ring would have an infinite vertical acceleration. Therefore, $\hat{\boldsymbol{s}} = \hat{\boldsymbol{e}}_x$ at the trailing edge or, equivalently, $\partial_\alpha y(1, t) = 0$.

Although well known in classical mechanics, free-end boundary conditions have not been studied much in membrane (as opposed to beam/plate) flutter problems. Tamai, Murphy & Hu (2008) studied membrane wings with partially free trailing edges and found that trailing edge fluttering may occur at relatively low angles of attack. Another recent experimental study found that membrane wing flutter can be enhanced by the vibrations of flexible leading and trailing edge supports (Arbós-Torrent, Ganapathisubramani & Palacios 2013). Partially free edges occur also in sails: the shape of a sail membrane can be controlled by altering the tension in cables running along its free edges (the 'leech' and 'foot') (Kimball 2009). Flutter can occur when the tension in these edges is sufficiently low (Colgate 1996). A related application is to energy harvesting by membranes mounted on tensegrity structures (networks of rigid rods and elastic fibres) and placed in fluid flows (Sunny, Sultan & Kapania 2014; Yang & Sultan 2016). In such cases the membrane ends have some degrees of freedom akin to the free-end boundary conditions defined above.

https://doi.org/10.1017/jfm.2020.153 Published online by Cambridge University Press

We will show that free ends allow for a wide range of unsteady membrane dynamics, unlike in the fixed–fixed case. Related work has studied the dynamics and flutter of membranes and cables under gravity with free ends (Triantafyllou & Howell 1994; Manela & Weidenfeld 2017). Here we neglect gravity to focus specifically on the basic flutter problem (Shelley & Zhang 2011). Without gravity, some restriction on the motion of the free membrane ends is needed to avoid ill-posedness due to membrane compression (Triantafyllou & Howell 1994). This is provided by the vertical poles in figure 2. Although this type of free-end boundary condition has mainly been studied theoretically, it has been realized experimentally by Kashy *et al.* (1997), with the membrane represented by an extensional spring that is tethered by steel wires to vertical supports.

In the third case, 'free–free,' both ends are free: $\partial_\alpha y(-1, t) = \partial_\alpha y(1, t) = 0$. Here the membrane is perturbed differently: it is initially set with a small non-zero slope,

$$\zeta(\alpha, 0) = (\alpha + 1)(1 + \mathrm{i}\sigma) \tag{2.24}$$

for $\sigma = 10^{-3}$.

3. Numerical results and discussion

We now describe the range of dynamics of the extensible membrane with the three sets of boundary conditions. In each case, we first present the flutter stability region for the flat membrane in the R_1–T_0 plane (it is independent of R_3 because it depends only on the small-deflection behavior). We then consider the large-amplitude dynamics using three main quantities to characterize them. One is the time-averaged deflection of the membrane,

$$\langle y_{defl} \rangle \equiv \frac{1}{t_2} \int_{t_1}^{t_1+t_2} \left(\max_{-1 \leqslant \alpha \leqslant 1} y(\alpha, t) - \min_{-1 \leqslant \alpha \leqslant 1} y(\alpha, t) \right) \mathrm{d}t, \tag{3.1}$$

where t_1 and t_2 are sufficiently large (typically 50–100) that $\langle y_{defl} \rangle$ changes by less than 1 % with further increases in these values. Here $\langle y_{defl} \rangle$ is the maximum membrane deflection minus the minimum deflection, averaged over time.

The second quantity is the frequency, defined as the mean frequency in the power spectrum computed using Welch's method (Welch 1967). The power spectrum is obtained from a time series of the free sheet circulation when the membrane has reached steady-state large-amplitude dynamics. The third quantity is the time-averaged number of zero crossings along the membrane, computed with the same temporal data as the power spectrum. The number of zero crossings is a measure of the 'waviness' of the membrane shape.

3.1. *Fixed–fixed membranes*

We begin by presenting the dynamics of membranes with both ends fixed, the case considered by previous studies on membrane flutter. The most detailed linear stability analysis of the problem is by Tiomkin & Raveh (2017). Their model is essentially a linearized version of ours, and includes a flat vortex wake extending to infinity downstream. They find that all membranes become unstable when the pretension T_0 drops below a critical value $\approx$1.73, independent of R_1. A qualitatively similar result was found by Newman & Paidoussis (1991) for an infinite periodic membrane with no free vortex wake. Below the critical pretension, the membranes in Tiomkin & Raveh

https://doi.org/10.1017/jfm.2020.153 Published online by Cambridge University Press

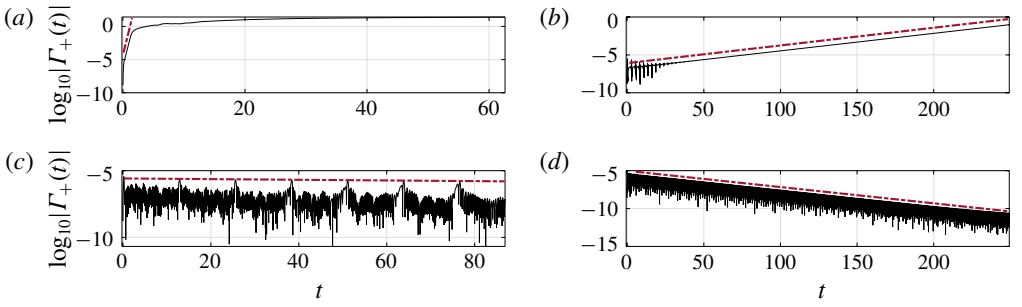


FIGURE 3. (Fixed–fixed) Examples of the $\log_{10}$ of the total wake circulation versus time with (*a*) $(R_1, T_0) = (10^{-1.8}, 10^{-1.2})$, (*b*) $(R_1, T_0) = (10^{-0.2}, 10^{0.2})$, (*c*) $(R_1, T_0) = (10^{2}, 10^{1})$ and (*d*) $(R_1, T_0) = (10^{1}, 10^{3})$. The growth/decay rates are given by the slopes of the dot–dashed red lines. In all cases we set $R_3 = 1$, but the linear growth rates are independent of R_3 (we show the R_3 term to be cubic in deflection in (3.2*a*,*b*), and, therefore, negligible in the linear growth regime).

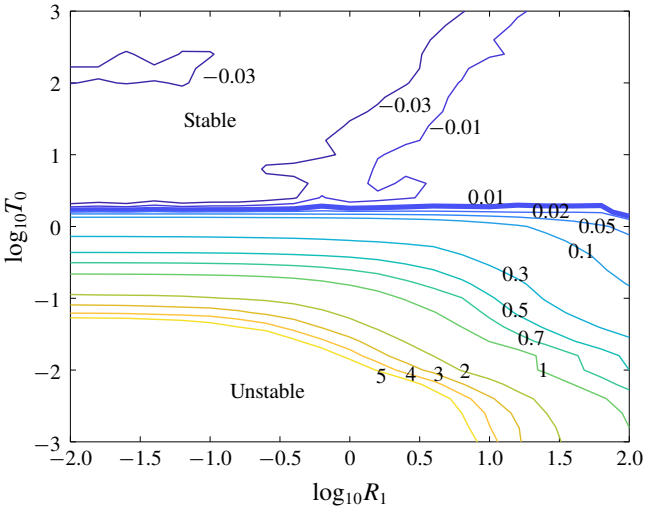


FIGURE 4. A contour plot of the exponential (base 10) growth and decay rates of wake circulation after a small transient perturbation, in the fixed–fixed case. The thicker line separates the stable and unstable cases.

(2017) lose stability by divergence (exponential growth of deflection) at small R_1 or by divergence with flutter (exponential growth with a complex growth rate, i.e. growth with oscillation) at large R_1.

We use our nonlinear simulation to compute the stability threshold for membranes by applying the small transient perturbation (2.23) at the leading edge and observing exponential growth (followed by large-amplitude, nonlinear dynamics) or exponential decay in membrane deflection and wake circulation $\Gamma_+(t)$. Examples are shown in figure 3. For the stability results presented in figures 3 and 4, we use (2.23) with $\sigma = 10^{-6}$.

We compute the growth and decay rates of the initial perturbation from data analogous to those in figure 3, on a fine grid of values in the R_1–T_0 space spanning

https://doi.org/10.1017/jfm.2020.153 Published online by Cambridge University Press

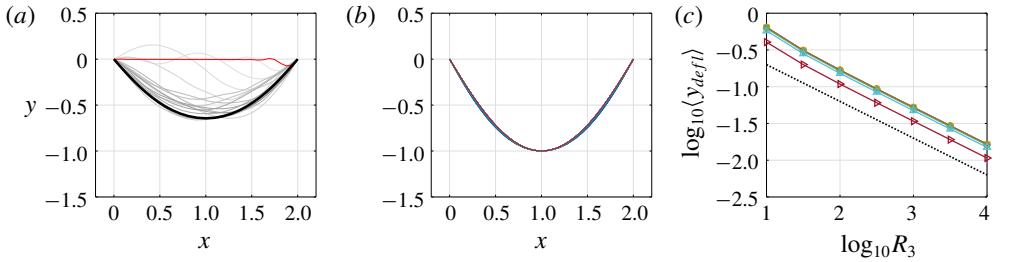


FIGURE 5. Fixed–fixed membrane shapes. (*a*) For $R_1 = 10^{-0.5}$, $R_3 = 10^1$ and $T_0 = 10^{-3}$ the membrane shapes at $t = 1$ (red), $1.5, 2.5, 3.5, 4.5, \ldots, 16.5$ (light gray to black). (*b*) Steady membrane shapes at late times, with y coordinates scaled by maximum deflection, for R_3 ranging from 10^1 to 10^4 and T_0 ranging from 10^{-3} to 1. (*c*) The maximum membrane deflection at steady state versus the stretching modulus R_3.

several orders of magnitude in each parameter. We show in figure 4 a contour plot of the growth/decay rates, i.e. β in the early time interval, where $\Gamma_+(t) \approx K\, 10^{\beta t}$ for some constant K. Values (well) above 5 occur in the lower-left corner, but are omitted for visual clarity. Above a critical pretension $T_0 \approx 1.78$ the membranes are stable, with small transient deflections decaying to the flat state. Below the critical pretension, we have a divergence instability: small transient deflections grow exponentially at a rate that is purely real. Tiomkin & Raveh (2017) found a critical pretension of 1.73 in a slightly different model; unlike that study, we do not find evidence of neutral flutter or divergence with flutter in the fixed–fixed case at any R_1. The main differences are that our wake length grows from zero while that in Tiomkin & Raveh (2017) is infinite, and our model is a nonlinear, unsteady version of that in Tiomkin & Raveh (2017).

During the initial stages of the divergence instability, the membrane deflection grows from small amplitude without change of shape. Nonlinearities become important when the amplitude reaches order one, and the membrane shape evolves to its eventual steady state. For the large-amplitude analysis of fixed–fixed membranes that follows, the small transient perturbation (2.23) applied at the leading edge is used with $\sigma = 10^{-4}$. In figure 5(*a*) we show a sequence of membrane snapshots during the nonlinear dynamics. The earliest shape (red) is similar to those during the linear instability, with the largest deflection near the trailing edge. Subsequent shapes (ranging from light to dark gray and black) show the evolution to the eventual steady state. The final membrane shape is nearly fore-aft symmetrical, similar to those in Newman & Low (1984), Tzezana & Breuer (2019), Waldman & Breuer (2013, 2017), Rojratsirikul, Wang & Gursul (2009) and Nardini *et al.* (2018). These works also discuss membrane dynamics at non-zero angle of attack with applications to lift and thrust generation by membrane airfoils (possibly heaving and/or pitching (Jaworski & Gordnier 2012)). Then vortices shed from the membrane's leading edge provide an unsteady forcing, causing membrane oscillations even in the fixed–fixed case. However, the present work is focused on the problem of membrane flutter at zero angle of attack, for which leading edge vortex shedding should be less significant. As for most vortex panel methods (Katz & Plotkin 2001), leading edge separation is difficult to represent in our model, so we focus on situations where trailing-edge vortex shedding is expected to be dominant, i.e. membranes at zero angle of attack with small-to-moderate deflections.

In figure 6 we show the late-time membrane shapes across several decades of R_3 and T_0. The shapes are all steady for $R_3 > 10^{0.5}$ (and, thus, independent of R_1 here,

https://doi.org/10.1017/jfm.2020.153 Published online by Cambridge University Press

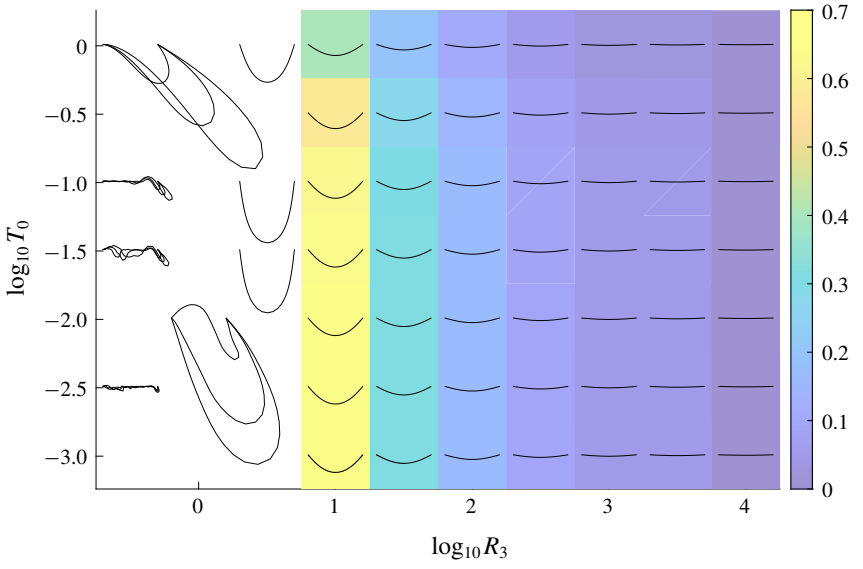


FIGURE 6. Membrane profiles in the fixed–fixed case, at steady state with moderate deflections (coloured background), or unphysically large or unsteady deflections (white background). In the unsteady cases a few snapshots at large times are shown. The colours show the deflection of the membrane (3.1). Here $R_1 = 10^{-0.5}$, but the steady shapes are independent of R_1, the dimensionless mass.

as the acceleration term in (2.8) is zero), but may oscillate chaotically for $R_3 \leqslant 10^{0.5}$, in which case a few snapshots are shown at late times. In these cases, the deflections are so large as to violate the assumption that vortex shedding is confined to the trailing edge, so we do not consider them further. For $R_3 > 10^{0.5}$, the colours show the maximum membrane deflection. At a given R_3, the deflection increases slightly as T_0 decreases from the stability threshold to ≈ 0.1, then converges as T_0 decreases further, the T_0 term becoming insignificant in the membrane equation (2.8). At a given T_0, the deflection decreases with increasing R_3 as a power law. In figure 5(*b*) we show that the shapes are almost identical, however, when the amplitudes are normalized. In figure 5(*c*) we show that the deflection $\langle y_{defl} \rangle \sim 1/\sqrt{R_3}$ (for $R_1 = 10^{-0.5}$ here, but these values are independent of R_1).

We explain how the scaling $\langle y_{defl} \rangle \sim 1/\sqrt{R_3}$ arises from the y-component of the membrane equation (2.8) with small deflections. We assume that $\partial_\alpha y \ll 1$ and $\partial_\alpha x \approx 1$. Then $\partial_\alpha s - 1 = \sqrt{(\partial_\alpha x)^2 + (\partial_\alpha y)^2} - 1 \approx \partial_\alpha y^2/2$ and $\hat{s}_y \approx \partial_\alpha y$. With these approximations, the y-components of the T_0 and R_3 terms in (2.8) are linear and cubic in deflection, respectively:

$$\partial_\alpha (T_0 \hat{s}_y) \approx T_0 \partial_{\alpha\alpha} y; \quad \partial_\alpha (R_3 (\partial_\alpha s - 1)\hat{s}_y) \approx R_3 \partial_\alpha ((\partial_\alpha y)^3/2). \tag{3.2a,b}$$

The R_1 term (multiplying $\partial_{tt} y$) is also linear in deflection (and zero here at steady state, but not for the oscillating membranes considered later). The pressure jump is linear in the bound vortex sheet strength because the left-hand side of (2.19) $\approx \partial_t \gamma + \partial_\alpha \gamma$ with small deflections. The bound vortex sheet strength is linear in the deflection by

https://doi.org/10.1017/jfm.2020.153 Published online by Cambridge University Press

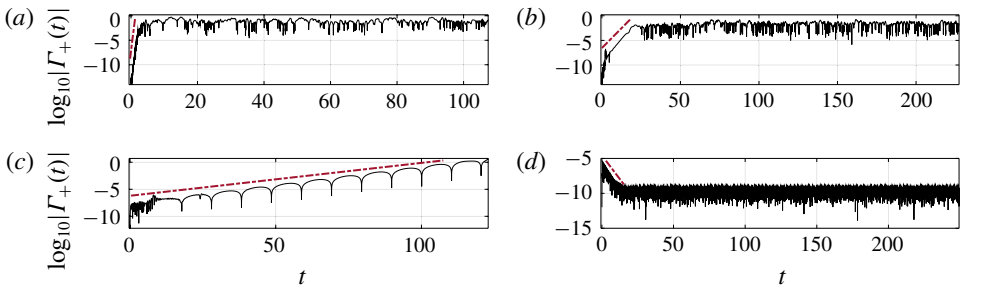


FIGURE 7. (Fixed–free) Examples of the total wake circulation versus time for $R_3 = 1$ on a log scale, with (*a*) $(R_1, T_0) = (10^{-3}, 10^{-2.8})$, (*b*) $(R_1, T_0) = (10^{-1.4}, 10^{-1.4})$, (*c*) $(R_1, T_0) = (10^{1}, 10^{-0.2})$ and (*d*) $(R_1, T_0) = (10^{-0.8}, 10^{2.2})$. The slopes of the dot–dashed red lines give the growth/decay rates. Recall that R_1 is the dimensionless membrane mass, T_0 is the dimensionless pretension and R_3 is the dimensionless stretching modulus.

the linearized version of (2.14),

$$\partial_t y(\alpha, t) \approx \frac{1}{2\pi} \fint_{-1}^{1} \frac{\gamma(\alpha', t)}{x(\alpha, t) - x(\alpha', t)} \, \mathrm{d}\alpha' - \frac{1}{2\pi} \int_0^{\Gamma_+(t)} \frac{x(\alpha, t) - x(\Gamma', t)}{(x(\alpha, t) - x(\Gamma', t))^2 + \delta(\Gamma', t)^2} \, \mathrm{d}\Gamma', \tag{3.3}$$

in which the second integral consists of bound vorticity advected from the trailing edge, so it has the same dependence on deflection as the bound vorticity. Here, with small deflections, we have assumed that $\partial_\alpha x \approx 1$, and then the linearization is the same as in Alben & Shelley (2008). Without viscous stresses, horizontal membrane deformations arise only through nonlinear terms in the elastic and pressure forces associated with large deflections, so it is reasonable to neglect them, and this is consistent with the simulation results. Balancing the terms that are linear in deflection with the product of R_3 and a term that scales with deflection cubed gives $\langle y_{defl} \rangle \sim 1/\sqrt{R_3}$.

3.2. *Fixed–free membranes*

We now investigate membranes with the leading edge fixed and the trailing edge free to move vertically (with $\partial_\alpha y = 0$ there – an extra equation that determines $y(1, t)$, now an extra unknown). With the free end, the membrane has a wide range of unsteady dynamics with small and moderate amplitude, unlike in the fixed–fixed case, and similar in some respects to the fixed–free flag with bending rigidity (Alben & Shelley 2008).

In figure 7 we show examples of the growth of wake circulation in time after small transient perturbations, analogous to figure 3. As before, for the analysis of the small-amplitude dynamics, we use (2.23) with $\sigma = 10^{-6}$. The main novelty is panel (*c*), an example of divergence with flutter – shown by the regularly spaced vertical asymptotes in the logarithm of wake circulation, corresponding to an oscillatory component – exponential growth with a complex growth rate.

We show in figure 8 a contour plot of the growth/decay rates and stability boundary in R_1–T_0 space, analogous to figure 4. Notable differences are that the stability boundary now varies with R_1. The critical pretension is close to that in figure 4 at the largest R_1, but decreases as R_1 decreases, and eventually reaches a lower plateau at $R_1 \ll 1$. The red triangles in figure 8 show cases like figure 7(*c*), membranes that become unstable through flutter and divergence.

https://doi.org/10.1017/jfm.2020.153 Published online by Cambridge University Press

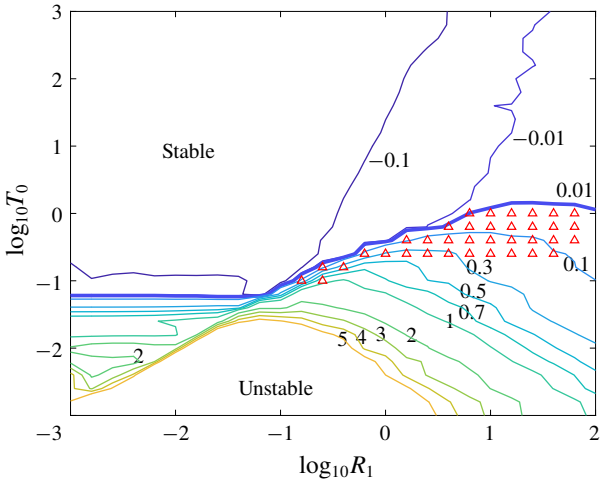


FIGURE 8. A contour plot of the exponential (base 10) growth and decay rates of wake circulation after a small transient perturbation, in the fixed–free case. The thicker line separates the regions where the membranes are stable and unstable. Growth rates (well) above 5 occur at the lower left but are omitted for visual clarity.

The membranes in the unstable region of figure 8 eventually reach large amplitudes, where nonlinearities (e.g. the R_3 term) determine the eventual steady-state motion. With fixed–free boundary conditions, oscillatory motions are typical, unlike for the fixed–fixed case. As for the fixed–fixed case, unrealistically large deflections occur for $R_3 \leqslant 1$, so we focus on $R_3 \gtrsim 1$.

Now we study the large-amplitude dynamics and we use $\sigma = 10^{-4}$ in (2.23). In figure 9 we show typical membrane snapshots in the unstable region of R_1–T_0 space from figure 8. At each (R_1, T_0) value, the set of snapshots is normalized by the maximum deflection of the snapshots to show the motions more clearly and scaled to fit within a coloured rectangle at the (R_1, T_0) value. Each snapshot has the corresponding R_1 value at its horizontal midpoint, and the T_0 value at its leading edge. Here R_3 is fixed at $10^{1.5}$, a value giving moderately large deflections for the steady-state motion. The colours denote the average deflection of the membrane (3.1).

The motions in figure 9 have the largest deflection amplitudes and smallest spatial frequency components at the largest $R_1(10^{1.5})$. Intuitively speaking, large R_1 (membrane inertia) allows the membrane to maintain its momentum for longer times against restoring fluid forces, and obtain larger deflections before reversing direction. The same has been observed for flutter with bending rigidity (Connell & Yue 2007; Alben & Shelley 2008). As R_1 decreases, the membrane deflection amplitudes progressively decrease and spatial frequencies increase until the motions become difficult to resolve numerically (to the left of the red vertical line). In this region, we find chaotic membrane oscillations with very small amplitudes and high spatial frequencies that become independent of R_1. When the number of points on the membrane is increased from 40 (here) to 80, 160 and 200, the membranes with $R_1 \leqslant 10^{-1}$ still oscillate chaotically but with even higher spatial frequency components, while those with $R_1 \geqslant 10^{-0.5}$ do not change significantly. Although the motions to the left of the red line are not converged with respect to the spatial grid, we retain their snapshots in figure 9 to indicate the behavior of the simulations. We find quasi-periodic motions in a finite band of R_1 values between $10^{-0.5}$ and $10^{0.5}$. Above

https://doi.org/10.1017/jfm.2020.153 Published online by Cambridge University Press

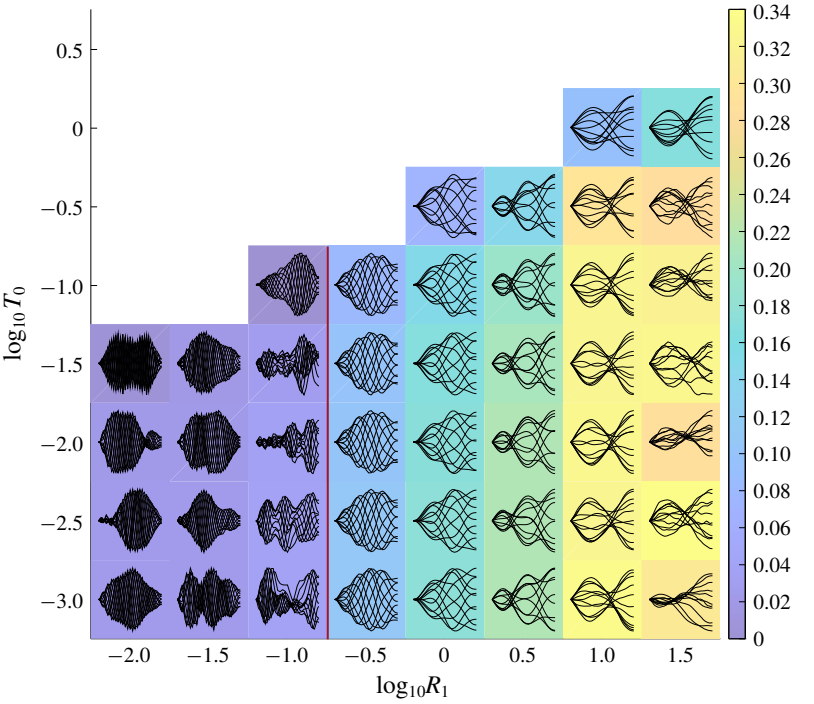


FIGURE 9. (Fixed–free) Snapshots of large-amplitude membrane motions in the unstable region of R_1–T_0 space for fixed $R_3 = 10^{1.5}$. Colours denote $\log_{10}$ of the average deflection defined by (3.1). At each (R_1, T_0) value, the set of snapshots is normalized by the maximum deflection of the snapshots to show the deformation modes more clearly and scaled to fit within a coloured rectangle at the (R_1, T_0) value.

and below this range, the motions become more irregular and chaotic, and more up–down asymmetrical at large R_1. The membrane motion depends weakly on T_0 except near the stability boundary (at the largest T_0 shown). At smaller T_0, the pretension does not affect the dynamics because it is negligible compared to the R_3 (stretching) term.

Next we look at the same quantities in a different two-dimensional slice through R_1–T_0–R_3 space. We fix $T_0 = 10^{-2}$ and in figure 10 show the membrane motions across R_1 and R_3. In the lower-right corner and at $(R_1, R_3) = (10^{-1}, 10^{0.5})$, snapshots are omitted because steady-state membrane motions were not obtained. We find that R_3 mainly affects the amplitudes of the snapshots, but not their shapes, particularly for the periodic motions with $R_1 = 10^{-0.5}$. The shapes do change noticeably for the more irregular and chaotic motions, which are sensitive to small changes in parameters, and near the smallest stretching modulus where steady-state motions occur, $R_3 \approx 10^{0.5}$.

We find that membranes with $R_1 = 10^{-0.5}$–$10^{0.5}$ move almost like traveling waves: their peaks and troughs translate downstream in forward time. Some of those with larger R_1 (10^1 and $10^{1.5}$) move approximately like standing waves, with a node and an antinode at certain locations. Similar dynamics have been found for fixed–fixed membranes perturbed by vortices shed from the leading edge (Song *et al.* 2008; Gordnier 2009; Timpe *et al.* 2013).

We show how the time-averaged deflection depends on R_3 at several fixed values of R_1 in figure 11. The plots follow the same $1/\sqrt{R_3}$ dependence at large R_3 as in the fixed–fixed case and for the same reason (explained in § 3.1).

https://doi.org/10.1017/jfm.2020.153 Published online by Cambridge University Press

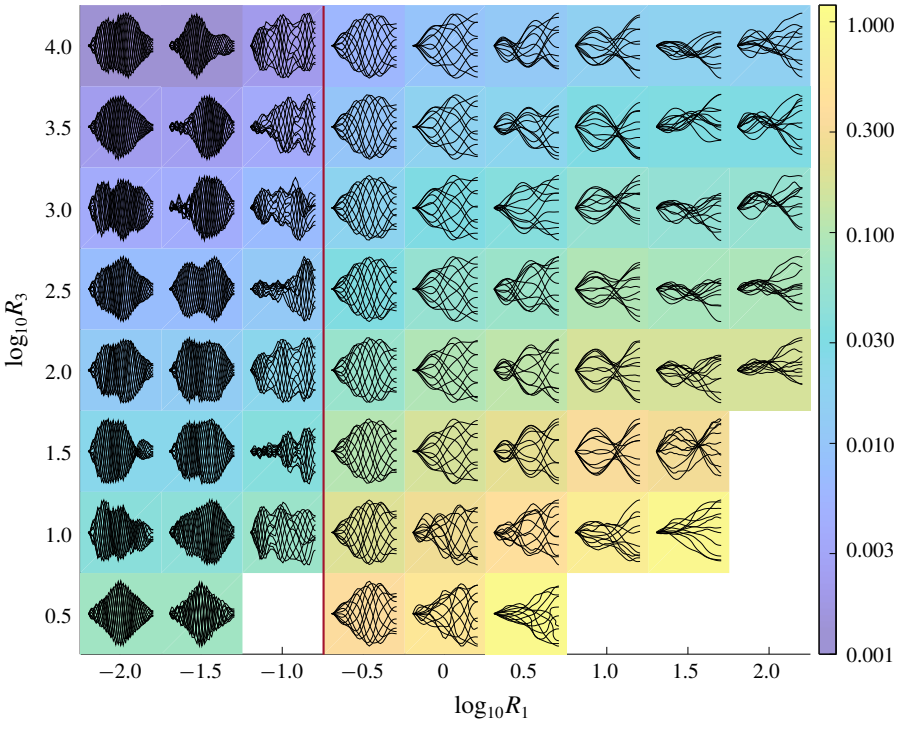


FIGURE 10. (Fixed–free) Snapshots of large-amplitude membrane motions in R_1–R_3 space for fixed $T_0 = 10^{-2}$. Colours denote $\log_{10}$ of the average deflection defined by (3.1). To the right of the vertical red dividing line the membrane motions are nearly periodic, but to the left of the red line the membrane oscillations are chaotic. At each (R_1, R_3) value, the set of snapshots is scaled to fit within a coloured rectangle at the (R_1, R_3) value and normalized by the maximum deflection of the snapshots to show the motions more clearly.

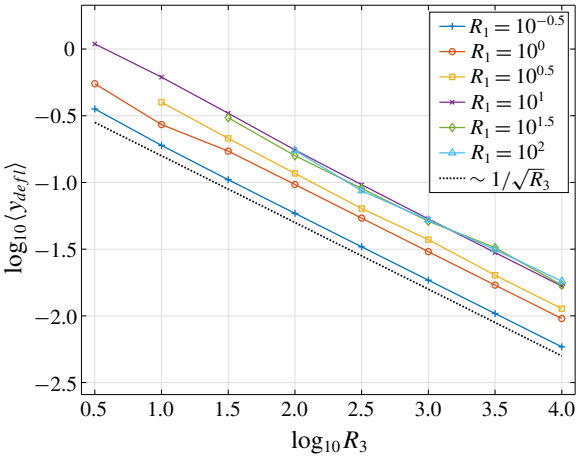


FIGURE 11. (Fixed–free.) Time-averaged deflections of the membranes (defined by (3.1)) versus R_3 for various R_1 and fixed $T_0 = 10^{-2}$. The black dashed line indicates the scaling $1/\sqrt{R_3}$.

https://doi.org/10.1017/jfm.2020.153 Published online by Cambridge University Press

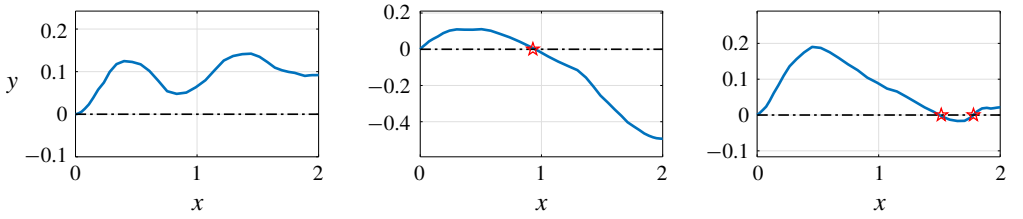


FIGURE 12. Examples of where zero crossings (red stars) are counted for model membranes (blue solid lines). Note that the leading edge of the membrane is not included as a zero crossing.

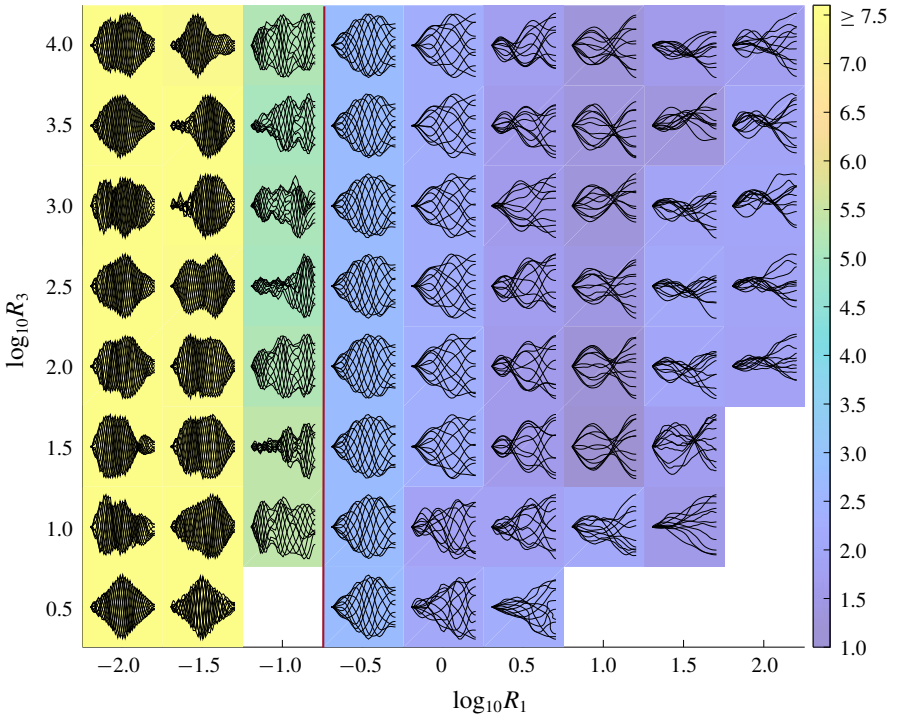


FIGURE 13. (Fixed–free.) Colours denote the time-averaged number of zero crossings for membrane flutter in the R_1–R_3 parameter space for fixed $T_0 = 10^{-2}$. In the lower-right corner and at $(R_1, R_3) = (10^{-1}, 10^{0.5})$, snapshots are omitted because steady-state membrane motions were not obtained. Note that R_1 is the dimensionless membrane mass, T_0 is the dimensionless pretension and R_3 is the dimensionless stretching modulus. At each (R_1, R_3) value the set of snapshots is normalized by the maximum deflection of the snapshots to show the motions more clearly.

In figure 10 we show the typical membrane motions at various R_1 and R_3 at fixed T_0 (and the phenomena are similar at other T_0 that yield flutter). We now quantify the membrane shapes in terms of the time-averaged number of 'zero crossings' – the number of times the membrane crosses $y = 0$. This is one way to measure the 'waviness' of a shape which is not sinusoidal (so the wavelength is not well defined) (Alben & Shelley 2008; Alben 2015). In figure 12 we show examples of shapes with zero, one, and two zero-crossings, respectively.

https://doi.org/10.1017/jfm.2020.153 Published online by Cambridge University Press

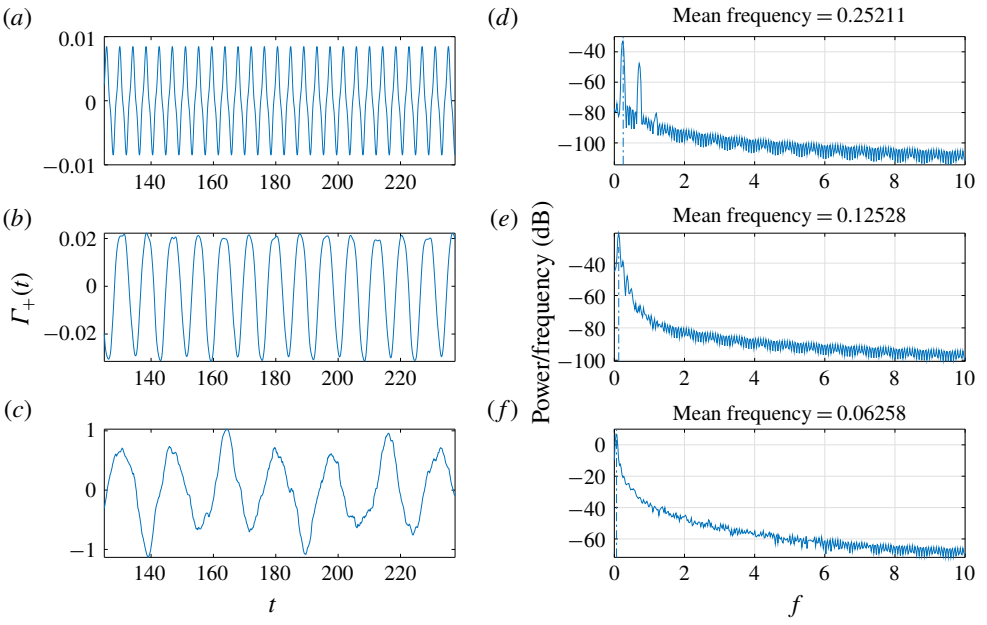


FIGURE 14. (Fixed–free.) A portion of the time series of total wake circulation $\Gamma_+(t)$ (*a–c*) and corresponding power spectra (*d–f*) for membranes with increasing mass density R_1 from top to bottom: (*a*,*d*) $(R_1, R_3) = (10^{-0.5}, 10^2)$, (*b*,*e*) $(R_1, R_3) = (10^{0.5}, 10^{3.5})$ and (*c*,*f*) $(R_1, R_3) = (10^{1.5}, 10^{1.5})$. In all cases $T_0 = 10^{-2}$.

We have already mentioned the trend to higher spatial frequency components with decreasing R_1. In figure 13 we quantify this relationship by showing the average number of zero crossings for the same snapshots in figure 10 (where the deflection amplitude was plotted). Decreasing R_1 from the largest value (10^2), the average number of zero crossings actually decreases slightly to about 1 near 10^1, and then increases with further decreases in R_1 as the motions become more periodic and then more irregular at yet smaller R_1, where the motions are not fully resolved spatially.

The temporal dynamics corresponding to these motions are quantified by computing the power spectra of time series of the total wake circulation, $\Gamma_+(t)$. In figure 14 we show examples of the time series of $\Gamma_+(t)$ that correspond to the different types of power spectra. Panel (*a*) shows an example with a periodic motion at $R_1 = 10^{-0.5}$. The corresponding $\Gamma_+(t)$ is periodic though not sinusoidal, resulting in a sequence of sharp peaks in the power spectrum. Panel (*b*) shows a less periodic response at larger R_1, still dominated by a single frequency but with clear variations from one cycle to the next. In panel (*c*) at still larger R_1, the trend toward aperiodicity continues. Nonetheless, the time series (left) shows peaks with a somewhat regular spacing. The corresponding power series (right) has a single peak close to zero frequency and a gradual decay in the power spectrum at higher frequencies, typical of chaotic dynamics.

In figure 15 we show these spectra, computed using Welch's method (Welch 1967), across R_1–R_3 space with $T_0 = 10^{-2}$. The colours denote the mean frequencies, i.e. the first moments of the power spectra, normalized by total power. As R_1 increases from $10^{-0.5}$ to 10^2 and the dynamics change from periodic to chaotic, the power spectra change as described in the previous figure, with little dependence on R_3 except at the

https://doi.org/10.1017/jfm.2020.153 Published online by Cambridge University Press

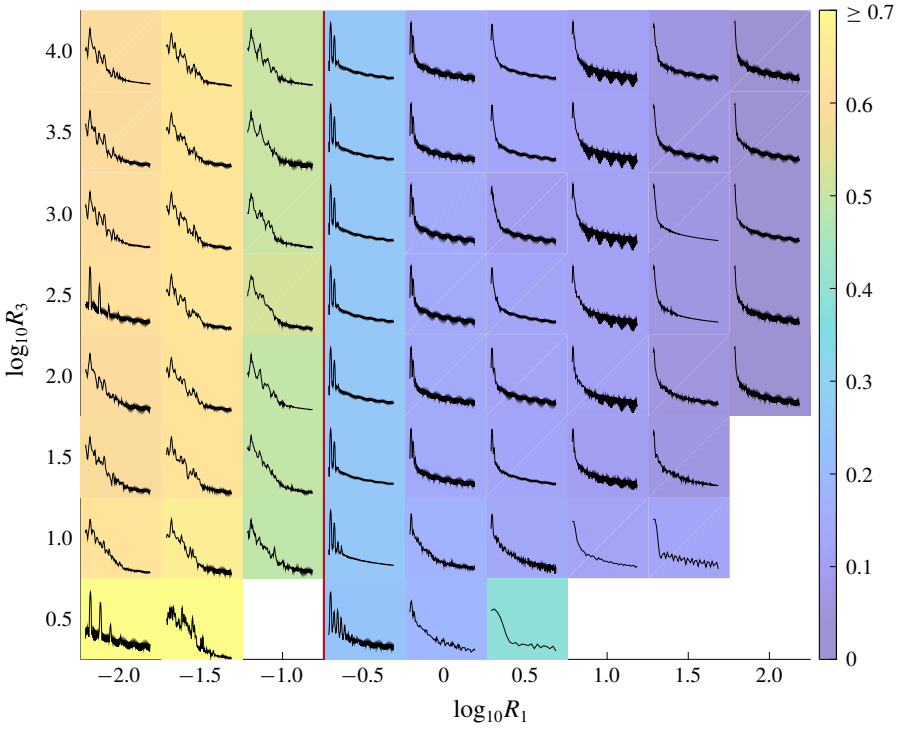


FIGURE 15. Colours denote the mean frequencies of large-amplitude motions in the fixed–free case for various R_1 and R_3, all with $T_0 = 10^{-2}$. The corresponding power spectra for each membrane are plotted in black. In the lower-right corner and at $(R_1, R_3) = (10^{-1}, 10^{0.5})$, power spectra are omitted because steady-state membrane motions were not obtained. Each power spectrum is a plot of power density (per unit frequency) versus frequency as in the right-hand side panels of figure 14. The axis scales are omitted due to space constraints but our focus here is on the qualitative features only.

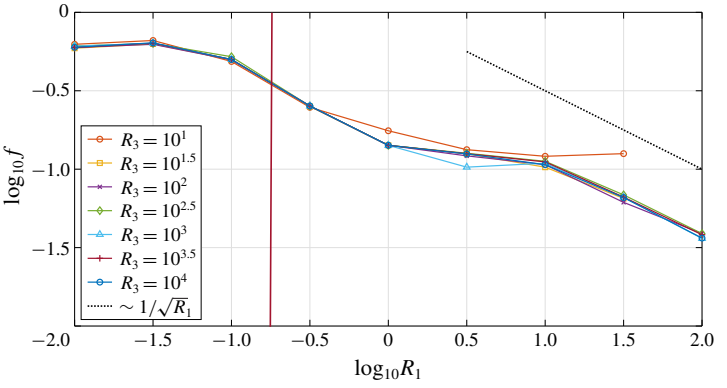


FIGURE 16. (Fixed–free) Plots of the mean frequency $\log_{10} f$ versus mass density $\log_{10} R_1$ with various R_3 and fixed $T_0 = 10^{-2}$. The black dashed line shows the scaling $1/\sqrt{R_1}$.

https://doi.org/10.1017/jfm.2020.153 Published online by Cambridge University Press

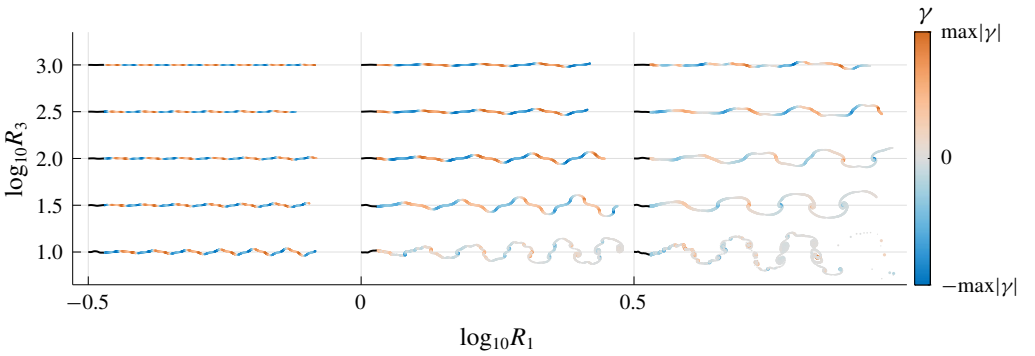


FIGURE 17. (Fixed–free) Snapshots of the membrane motion (in black) and the vortex wake in a portion of the R_1–R_3 parameter space for fixed $T_0 = 10^{-2}$. In each case the (R_1, R_3) values are marked at the left endpoint of the membrane. The wake is colour-coded according to the vortex sheet strength at the last time step. It is also thickness-coded according to $15|\gamma|^{1/3}$. Counterclockwise rotating vortices are shown in orange and clockwise rotating vortices in blue. For example, for $(R_1, R_3) = (10^{-0.5}, 10^3)$, we have $\max|\gamma| = 0.0041$ and for $(R_1, R_3) = (10^{0.5}, 10^1)$, we have $\max|\gamma| = 1.9$.

lowest values. The mean frequencies decrease by about a factor of five. Thus, there is a strong correlation between the number of zero crossings (or flutter mode) and oscillation frequency, as has been seen previously in flag flutter problems (Shelley *et al.* 2005; Eloy *et al.* 2007; Alben & Shelley 2008; Alben 2015). The two are in linear proportion for the modes of the linear wave equation for a membrane in a vacuum (Graff 1975; Farlow 1993). The power spectra to the left of the red line (for motions which are not converged with respect to grid spacing) show higher frequencies and a broadband response, reflecting chaotic dynamics.

In figure 16 we show more quantitatively how the mean frequency varies with parameters. There is very little dependence on R_3 except near the smallest R_3, where stable motions can be computed, $\approx 10^1$. There is a steady decrease from $R_1 = 10^{-1}$ to 10^0 followed by a small plateau for $10^0 \leqslant R_1 \leqslant 10^1$, and another decrease within $10^1 \leqslant R_1 \leqslant 10^2$. The trend at the largest R_1 is well approximated by $f \sim 1/\sqrt{R_1}$ (admittedly over a short range of R_1), except at the two smallest R_3 values. This scaling arises when one approximates the normal component of the membrane equation (2.8) by its y-component, and chooses a characteristic time scale t_0 so that $R_1 \partial_{tt} y$ balances other terms that depend on y but not its time derivatives (i.e. the R_3 and T_0 terms and some of the fluid pressure terms). At large R_1, $R_1 \partial_{tt} y$ is comparable to the other terms when $R_1/t_0^2 \sim 1$ or $t_0 \sim \sqrt{R_1}$, giving a typical frequency $f_0 \sim 1/\sqrt{R_1}$.

We have mainly focused on the membrane dynamics, but we conclude this section by briefly considering the vortex sheet wake dynamics. In figure 17 we show snapshots of vortex wakes in a small portion of R_1–R_3 space, where the membranes' motions transition from small to large amplitudes. At smaller amplitudes (top and left), the wakes are mostly flat (despite the complexity of the corresponding membrane snapshots, shown in figure 10) and have periodic undulations, as the membrane motions are approximately periodic at these parameters. Here the vorticity is weak, so there is little vortex wake roll-up before the wake is advected many body lengths downstream by the background flow. With smaller membrane deflections, we observe two pairs of oppositely signed vortices per flapping period ($R_1 = 10^{-0.5}$ with $R_3 = 10^1$–10^3, and $R_1 = 10^0$ with $R_3 = 10^{1.5}$–10^3), akin to a 2P wake (Williamson &

https://doi.org/10.1017/jfm.2020.153 Published online by Cambridge University Press

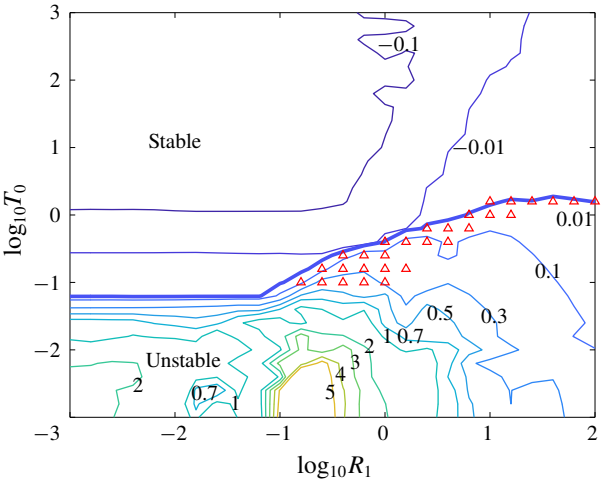


FIGURE 18. A contour plot of the exponential (base 10) growth and decay rates of wake circulation after a small transient perturbation, in the free–free case. The thicker line separates the stable membranes from the unstable ones.

Roshko 1988). At larger deflections, there is more roll-up and the wake resembles a von Kármán vortex street in some cases ($R_1 = 10^{0.5}$ with $R_3 = 10^{1.5}$–$10^{2.5}$), or a less regular wake with many spirals per flapping period (bottom right, $R_1 = 10^{0}$–$10^{0.5}$ with $R_3 = 10^{1}$). In general, the wake is spatially periodic to the extent that the membrane motion is temporally periodic. The more irregular wakes reflect the greater aperiodicity of the membrane motion at large amplitudes.

3.3. *Free–free membranes*

We have seen that changing the trailing edge boundary condition from fixed to free dramatically changes the membrane dynamics, from static deflections with a single maximum to a wide range of oscillatory modes that have some commonalities with flapping plates and flags (Shelley & Zhang 2011). Therefore, it is natural to consider the effect of making both ends free, and determine if the membrane dynamics undergo further dramatic changes. Computationally, the method is the same as before, but the system of unknowns now includes the values of y at both endpoints, corresponding to the two equations $\partial_\alpha y(-1, t) = \partial_\alpha y(1, t) = 0$.

The contour plot of growth/decay rates of the initial perturbation ((2.24) with $\sigma = 10^{-3}$) is shown in figure 18. It is similar to that in the fixed–free case (figure 8), particularly in the location of the stability boundary and the contours in the stable region. In the unstable region, the growth rates are significantly smaller and there are slight differences in where divergence with flutter occurs (red triangles).

We now consider the large-amplitude membrane motions in R_1–R_3 space with T_0 fixed at 10^{-2}, the free–free analog of figure 10. In figure 19 we show the motions superposed on a colour field that labels the time-averaged membrane deflections (3.1). The membrane is now free to translate in the y-direction, which leads to additional complexities in the motions. As in the fixed–free case (figure 10), increasing R_3 decreases the deflections of the snapshots without significantly changing the qualitative features of their shapes. Decreasing R_1 generally decreases the deflections also, except near the largest R_1. The membranes mostly oscillate within a fixed vertical region,

https://doi.org/10.1017/jfm.2020.153 Published online by Cambridge University Press

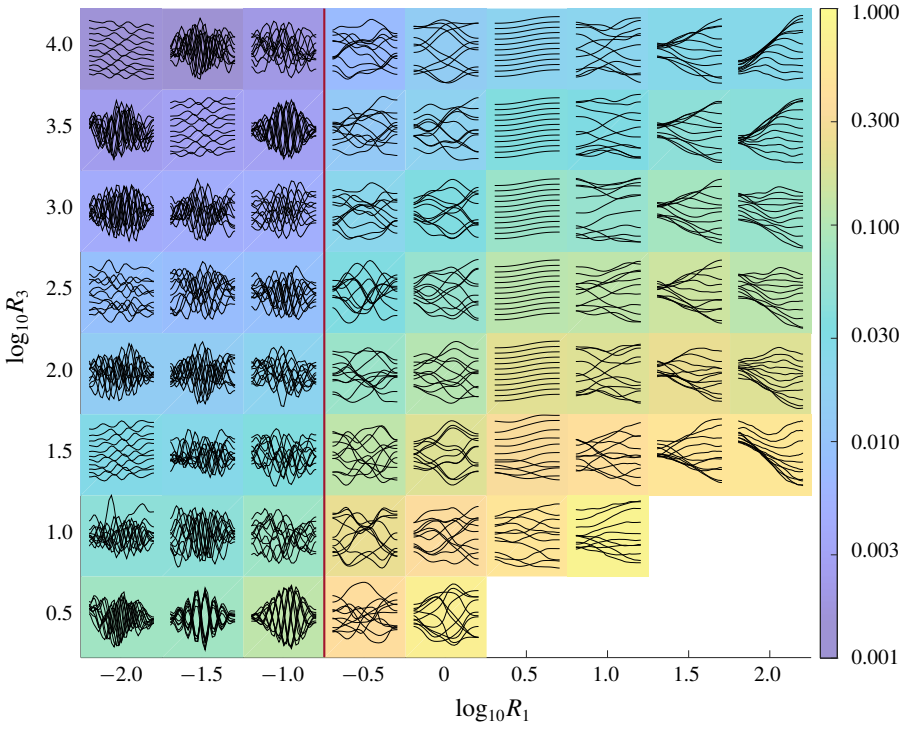


FIGURE 19. Membrane snapshots in the free–free case superposed on colours labeling the time-averaged deflection for each (R_1, R_3) pair with $T_0 = 10^{-2}$ defined by (3.1). Recall that R_1 is the dimensionless membrane mass, T_0 is the dimensionless pretension and R_3 is the dimensionless stretching modulus. At each (R_1, R_3) value, the set of snapshots is scaled to fit within a coloured rectangle at the (R_1, R_3) value and normalized by the maximum deflection of the snapshots to show the motions more clearly.

except at $R_1 = 10^{0.5}$, where the membranes mostly translate steadily in y, and with a steady shape. The membranes are somewhat straighter than in the fixed–free case, possibly because their translational freedom allows them to align more closely with the oncoming flow. As R_1 decreases below $10^{0.5}$, the membranes develop sharper curvatures until they again become difficult to resolve numerically at and below 10^{-1}. To the left of the red dividing line, increasing the number of points on the membrane leads to similarly complex oscillatory motions with somewhat sharper curvatures in most cases.

To show the net translational motions of the membranes, we plot in figure 20 the y coordinates of the membranes' midpoints over time. The colour denotes the net y displacement up to $t = 250$. At $R_1 = 10^2$, the membranes' translational motions are generally oscillatory with long time intervals between changes in vertical direction. Decreasing R_1 generally decreases the lengths of these intervals, corresponding to higher frequency translational motions. At $R_1 = 10^{0.5}$, the membranes translate steadily (with occasional changes in direction, at $R_3 = 10^1$ and $10^{1.5}$). We find that steady (or nearly steady) translational motions actually occur at various R_1 in the range $(10^{0.4}, 10^1)$. At $R_1 = 10^0$, essentially periodic trajectories occur (at this R_1, periodic motions were also seen in the fixed–free case, figure 10). Decreasing R_1 to $10^{-0.5}$, we have many cases of oscillation superposed on a steady (or somewhat meandering)

https://doi.org/10.1017/jfm.2020.153 Published online by Cambridge University Press

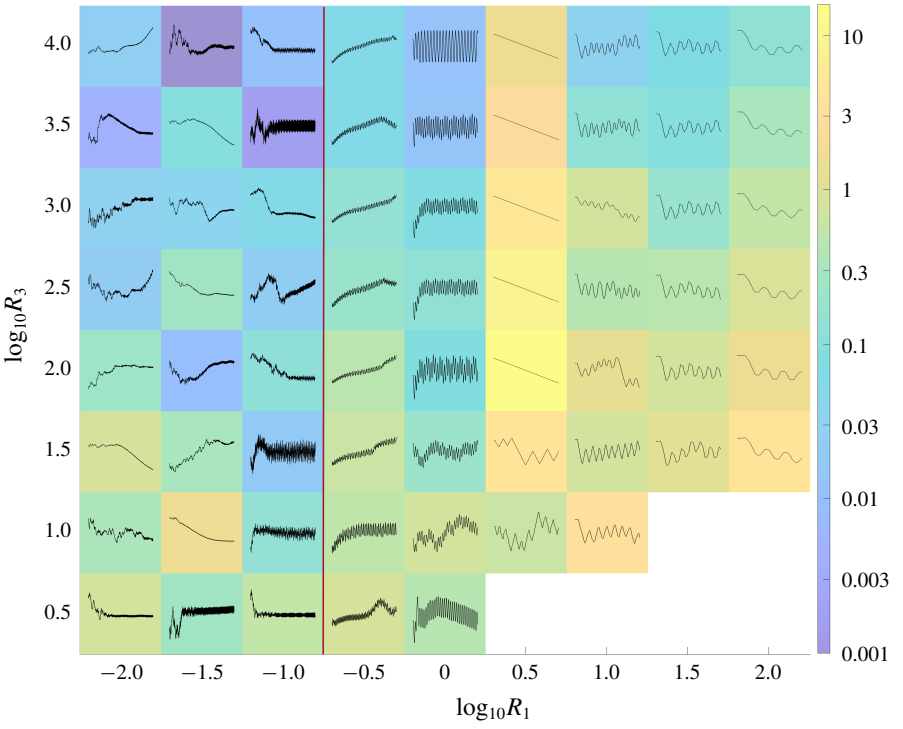


FIGURE 20. Time series of the y coordinates of the free–free membranes' midpoints, superposed on colours giving the maximum values of the time series for each (R_1, R_3) pair with $T_0 = 10^{-2}$. In the lower-right corner, data are omitted because long-time trajectories were not obtained. For each membrane's midpoint y-coordinate time series, the axis scales are omitted due to space constraints, but our focus here is on the qualitative features only.

translation. This trend continues to the left of the red line, where the solutions become difficult to resolve numerically. The net membrane translations generally decrease with increases in R_3, presumably because the membranes are flatter, so they have a more tangential motion with respect to the oncoming flow if their vertical translations are smaller, and tangential motions are not resisted in this inviscid model.

We can use the power spectra of the total wake circulation to again characterize the membranes' temporal dynamics in the same R_1–R_3 parameter space. We find properties that are similar to the fixed–free case: low frequency, somewhat aperiodic motions at the largest R_1, and a steady transition to higher-frequency motions with decreasing R_1 until, near $R_1 = 10^{0.5}$, the steady motions appear which have only a zero-frequency component in the wake circulation (the total wake circulation decays to zero in these cases). At $R_1 = 10^0$, periodic motions appear, and then become increasingly aperiodic with further decreases in R_1. The diverse types of translational motions do not lead to large qualitative changes in the power spectra, except for the steadily translating motions. We present power spectrum data for the free–free case in appendix C.

When both membrane ends are free, the 'waviness' of the membrane is more difficult to define. Our definition is the number of crossings that a membrane makes with the line connecting its two endpoints, averaged over time. A definition based on crossings of a horizontal line would ignore the fact that many of the

https://doi.org/10.1017/jfm.2020.153 Published online by Cambridge University Press

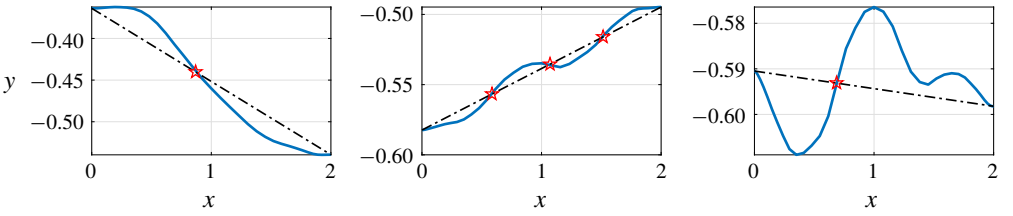


FIGURE 21. Schematic diagram that explains the term zero crossings for a membrane with both endpoints free. The dot–dashed black line is the linear line that connects the two endpoints of the membrane at each time step, the blue solid line resembles the membrane at an instant of time, and the red star denotes the zero-crossing, which is the intersection point between the linear line and the membrane profile.

free–free membranes have small undulations about a line with non-zero net slope. The combination of a steady background flow with a nearly steady vertical translation makes a line with non-zero slope the state of pure tangential motion relative to the fluid, and, thus, the basic state of minimal resistance to the fluid. In figure 21 we illustrate the zero crossings using this definition for several membrane examples. We omit the two endpoints from the set of zero crossings.

In figure 22 we show the average number of zero crossings in the R_1–R_3 space already discussed. Like the power spectra, this measure of membrane motion filters out some of the differences in translational motion. Starting at $R_1 = 10^2$, the number of zero crossings decreases to about two for the steady translating motions near $R_1 = 10^{0.5}$, and then increases with further decreases in R_1 as the motions become more periodic and then more irregular at yet smaller R_1, where the motions are not fully resolved spatially. The trend is generally the same as in the fixed–free case.

Examples of vortex wakes in the free–free case are shown in figure 23. The wakes have oscillatory patterns like those in the fixed–free case (figure 17). Here, however, the membranes' translational motion leads to more complexity in the wakes' spatial configurations. Fewer of these cases resemble a von Kármán vortex street than those in the fixed–free case. For example, the membrane with $R_1 = 10^0$ and $R_3 = 10^{0.5}$ in figure 22 oscillates almost periodically in the y direction. The motion is shown enlarged in figure 24(*a*). The corresponding vortex wake, shown in figure 23 (middle column, bottom row) is more complex than a von Kármán vortex street. At the upper right of figure 23 are approximately straight-line wakes, corresponding to membranes that translate steadily with a constant shape, e.g. the enlarged example in figure 24(*b*). Here the vortex wakes have zero strength density in the large-time limit, and so they translate steadily downstream without any self-induced undulatory motion or roll-up.

Our final results are a brief comparison of membrane frequencies in the small-amplitude exponential growth regime, the focus of previous membrane flutter studies, and the large-amplitude steady-state regime. The top three rows of table 2 compare the small- and large-amplitude frequencies of three fixed–free membranes, shown in figure 9 (at $R_3 = 10^{1.5}$), that become unstable through flutter and divergence and oscillate with a single dominant frequency. The bottom two rows compare the frequencies for two free–free membranes that also oscillate with single dominant frequencies. We note that the frequency may become significantly lower or higher as the membranes transition from small to large amplitude. It is unclear in general if aspects of the large amplitude motion can be inferred from the shapes and frequencies of the unstable modes in the linearized, small-amplitude regime.

https://doi.org/10.1017/jfm.2020.153 Published online by Cambridge University Press

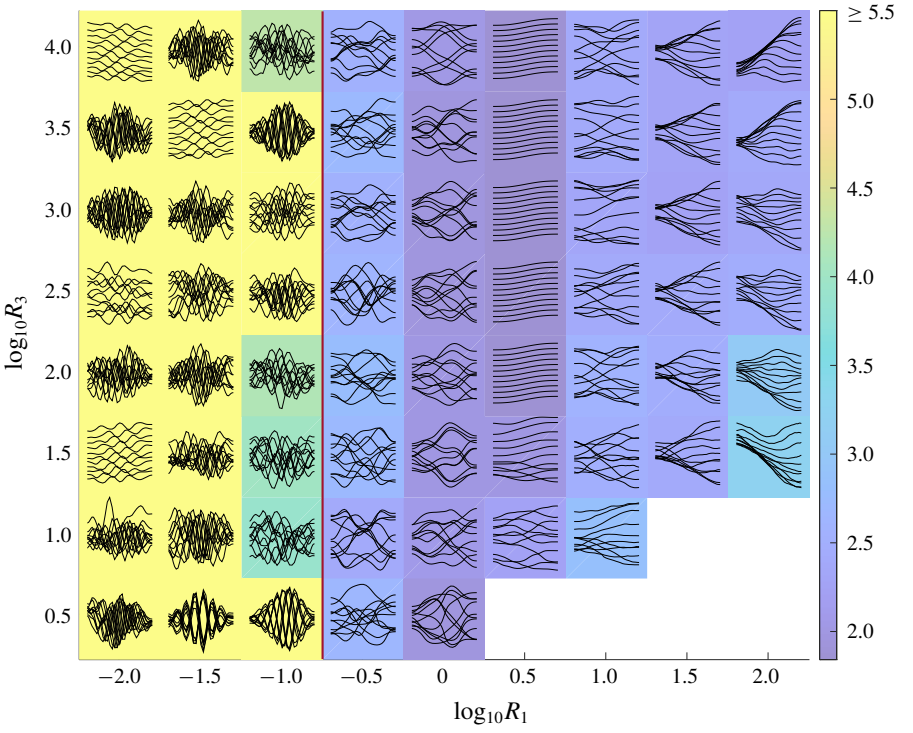


FIGURE 22. (Free–free) Snapshots of the membrane motion at the large-amplitude regime, plotted on top of colours that correspond to the number of zero crossings in the R_1–R_3 parameter space for fixed $T_0 = 10^{-2}$. The data in the right-bottom corner are obtained for a shorter time and so, we neglect the computational results for those values of R_1 and R_3. At each (R_1, R_3) value, the set of snapshots is scaled to fit within a coloured rectangle at the (R_1, R_3) value and normalized by the maximum deflection of the snapshots to show the motions more clearly.

	(R_1, T_0)	Small-amplitude frequency	Large-amplitude frequency
Fixed–free	$(10^{0}, 10^{-0.5})$	0.1717	0.1313
	$(10^{0.5}, 10^{-0.5})$	0.0970	0.1240
	$(10^{1.5}, 10^{0})$	0.0362	0.0543
Free–free	$(10^{0}, 10^{-0.5})$	0.1607	0.1303
	$(10^{1}, 10^{0})$	0.0241	0.0542

TABLE 2. Comparison of frequencies in the small-amplitude and large-amplitude regimes with $R_3 = 10^{1.5}$ for three pairs of (R_1, T_0) at the flutter and divergence region for fixed–free and free–free membranes.

4. Conclusions

In this work we have studied the flutter instability and large amplitude dynamics of thin membranes. These are made of elastic materials – e.g. rubber, textile fabric or the skin of swimming or flying animals – with Young's moduli sufficiently small that stretching provides the primary resistance to fluid forces and bending resistance is

https://doi.org/10.1017/jfm.2020.153 Published online by Cambridge University Press

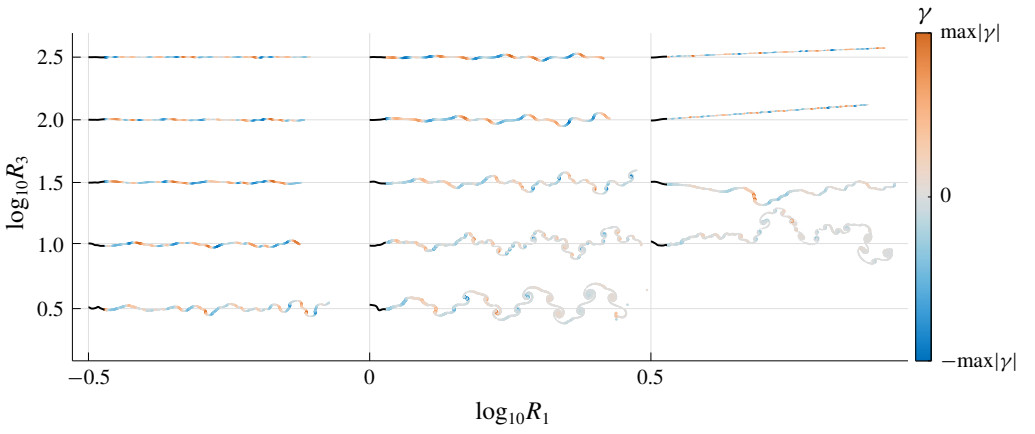


FIGURE 23. (Free–free) Snapshots of the membrane motion (in black) and the vortex wake in a portion of the R_1–R_3 parameter space for fixed $T_0 = 10^{-2}$. In each case the (R_1, R_3) values are marked at the left endpoint of the membrane. The wake is colour-coded according to the vortex sheet strength at the last time step. It is also thickness-coded according to $15|\gamma|^{1/3}$. Counterclockwise rotating vortices are shown in orange and clockwise rotating vortices in blue. For example, for $(R_1, R_3) = (10^{-0.5}, 10^{2.5})$, we have $\max|\gamma| = 0.0076$ and for $(R_1, R_3) = (10^{0.5}, 10^{1})$, we have $\max|\gamma| = 2.3$.

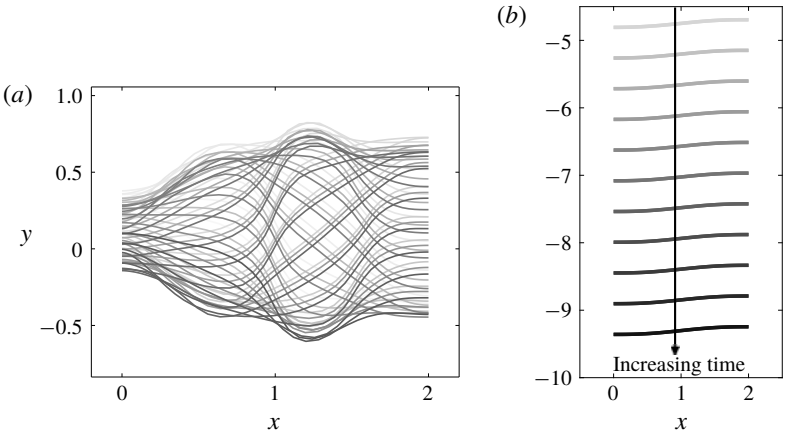


FIGURE 24. (Free–free) Membrane snapshots at the large-amplitude regime for (*a*) $R_1 = 10^0$ and $R_3 = 10^{0.5}$ and (*b*) $R_1 = 10^{0.5}$ and $R_3 = 10^{2.5}$. The shading of the membrane indicates the different phases in the motion, varying from gray at earlier times to black at current times.

negligible. Previous studies have considered the flutter instability of membranes with fixed ends. We find that all such membranes become unstable by divergence below a critical pretension T_0 close to the value identified in previous studies. Surprisingly, we find that all cases that exhibit large (but physically reasonable) deflections converge to states of steady deflection with single humps that are almost fore-aft symmetric, and the deflections scale as $1/\sqrt{R_3}$, where R_3 is the stretching modulus. These deformations are similar to those found with linearized models that assumed steady

https://doi.org/10.1017/jfm.2020.153 Published online by Cambridge University Press

deflection at a fixed angle of attack (Waldman & Breuer 2017; Tzezana & Breuer 2019).

We then considered membranes with the leading edge fixed and the trailing edge free, and found a wide range of unsteady dynamics, somewhat similar to those seen in studies of flapping plates or flags. The critical pretension T_0 now depends on the membrane mass density R_1. Membranes become unstable with divergence or with a combination of flutter and divergence in some cases near the stability boundary. The large-amplitude dynamics are independent of the pretension except close to the stability boundary, where the dynamics are in some cases more periodic and have smaller amplitudes. The dynamics depend most strongly on the membrane mass density R_1. At the largest R_1 studied we find the smallest oscillation frequencies and largest membrane deflections corresponding to somewhat chaotic and asymmetrical membrane motions. Here the mean temporal frequency scales as $1/\sqrt{R_1}$. As R_1 decreases, the membrane motions become more periodic and symmetrical, and with larger spatial frequency components (sharper curvatures and more zero crossings). At $R_1 \leqslant 0.1$ the motions become more chaotic again, with much finer spatial features that are difficult to resolve numerically.

With both edges free, the membrane motions show two new features – a vertical translational component that may be nearly steady or oscillatory, and a non-zero slope. The combination of the two yields a small angle of attack with respect to the oncoming flow. The translational motion may be steady, periodic or chaotic, and switch among these states with small changes of parameters. Superposed on the translational motions with non-zero slope are modes with oscillatory spatial and temporal features, similar to those in the fixed–free case in how they vary with T_0, R_1 and R_3.

Membrane (as opposed to beam/plate) flutter with free ends has barely been explored. However, our study shows that these boundary conditions allow for a much wider range of membrane dynamics with potential future applications in enhancing the performance of membrane wings (Tamai *et al.* 2008; Arbós-Torrent *et al.* 2013), sails (Colgate 1996; Kimball 2009), and energy harvesting by membranes mounted on tensegrity structures (Sunny *et al.* 2014; Yang & Sultan 2016). Extensional deformations may be used in conjunction with (Drachinsky & Raveh 2016; Chatterjee & Bryant 2018) or as an alternative to bending-dominated deformations for energy harvesting, e.g. the flutter of piezoelectric beams and bilayers (Erturk *et al.* 2010; Doaré & Michelin 2011; Giacomello & Porfiri 2011; Kim *et al.* 2013; Porfiri & Peterson 2013; Wang *et al.* 2016; Orrego *et al.* 2017).

Acknowledgements

We acknowledge support from a Rackham International Student Fellowship (University of Michigan) to C.M.

Declaration of interests

The authors report no conflict of interest.

Supplementary movies and materials

Supplementary movies and materials are available at https://doi.org/10.1017/jfm.2020.153.

https://doi.org/10.1017/jfm.2020.153 Published online by Cambridge University Press

Appendix A. Pressure jump equation

In this appendix we derive the equation for the pressure jump $[p](\alpha, t)$ across the membrane, given by (2.19), as in Alben (2012) but for an extensible body. We use vector notation instead of complex notation.

The Euler momentum equation given by

$$\partial_t \boldsymbol{u}(\boldsymbol{x}, t) + \boldsymbol{u}(\boldsymbol{x}, t) \cdot \nabla \boldsymbol{u}(\boldsymbol{x}, t) = -\nabla p(\boldsymbol{x}, t), \tag{A 1}$$

determines the velocity of the fluid flow $\boldsymbol{u}(\boldsymbol{x}, t)$ at a point $\boldsymbol{x}$ in the fluid. We want to calculate the fluid pressure at a point in the fluid that is adjacent to and follows a material point $\boldsymbol{X}(\alpha, t)$ on the membrane. The rate of change of fluid velocity at such a point is

$$\frac{\mathrm{d}}{\mathrm{d}t}\boldsymbol{u}(\boldsymbol{X}(\alpha, t), t) = \partial_t \boldsymbol{u}(\boldsymbol{x}, t)|_{\boldsymbol{x}=\boldsymbol{X}(\alpha,t)} + (\partial_t \boldsymbol{X}(\alpha, t) \cdot \nabla)\boldsymbol{u}(\boldsymbol{x}, t)|_{\boldsymbol{x}=\boldsymbol{X}(\alpha,t)}. \tag{A 2}$$

We replace the first term in (A 1) using the same term in (A 2) (the first term on the right-hand side). This yields the pressure gradient at a point that moves with $\boldsymbol{X}(\alpha, t)$. Since the fluid velocity is discontinuous across the membrane, we actually need to do this separately for points that tend toward $\boldsymbol{X}(\alpha, t)$ from each side of the membrane. We obtain

$$\frac{\mathrm{d}}{\mathrm{d}t}\boldsymbol{u}(\boldsymbol{X}(\alpha, t), t)^{\pm} + ((\boldsymbol{u}(\boldsymbol{x}, t) - \partial_t \boldsymbol{X}) \cdot \nabla \boldsymbol{u}(\boldsymbol{x}, t)|_{\boldsymbol{x}=\boldsymbol{X}(\alpha,t)})^{\pm} = -(\nabla p(\boldsymbol{x}, t)|_{\boldsymbol{x}=\boldsymbol{X}(\alpha,t)})^{\pm}, \tag{A 3}$$

using '+' for the side toward which the membrane normal $\hat{\boldsymbol{n}}$ is directed and '−' for the other side.

Next, we decompose the fluid velocity into components tangential and normal to the membrane. The normal component matches that of the membrane, v in (2.21*b*). The tangential component of the fluid velocity may be written in terms of its jump across the membrane, the same as the vortex sheet strength γ (Saffman 1992),

$$(\boldsymbol{u}^+ - \boldsymbol{u}^-) \cdot \hat{\boldsymbol{s}} = -\gamma, \tag{A 4}$$

and the average of the tangential components of the fluid velocity on the two sides of the membrane, denoted μ. Combining the tangential and normal components, we have

$$\boldsymbol{u}^{\pm} = \left(\mu \mp \frac{\gamma}{2}\right)\hat{\boldsymbol{s}} + v\hat{\boldsymbol{n}}. \tag{A 5}$$

We take the difference of (A 3) on the '+' and '−' sides:

$$\begin{aligned}&\frac{\mathrm{d}}{\mathrm{d}t}(\boldsymbol{u}^+(\boldsymbol{X}(\alpha, t), t) - \boldsymbol{u}^-(\boldsymbol{X}(\alpha, t), t)) + ((\boldsymbol{u}^+(\boldsymbol{x}, t) - \partial_t \boldsymbol{X}) \cdot \nabla \boldsymbol{u}^+(\boldsymbol{x}, t)|_{\boldsymbol{x}=\boldsymbol{X}(\alpha,t)}) \\ &\quad - ((\boldsymbol{u}^-(\boldsymbol{x}, t) - \partial_t \boldsymbol{X}) \cdot \nabla \boldsymbol{u}^-(\boldsymbol{x}, t)|_{\boldsymbol{x}=\boldsymbol{X}(\alpha,t)}) = -(\nabla p(\boldsymbol{x}, t)^+ - \nabla p(\boldsymbol{x}, t)^-)|_{\boldsymbol{x}=\boldsymbol{X}(\alpha,t)}.\end{aligned} \tag{A 6}$$

We then take the tangential component of (A 6), term by term. Using (A 5),

$$\hat{\boldsymbol{s}} \cdot \frac{\mathrm{d}}{\mathrm{d}t}(\boldsymbol{u}^+(\boldsymbol{X}(\alpha, t), t) - \boldsymbol{u}^-(\boldsymbol{X}(\alpha, t), t)) = \hat{\boldsymbol{s}} \cdot \partial_t(-\gamma(\alpha, t)\hat{\boldsymbol{s}}(\alpha, t)) = -\partial_t \gamma(\alpha, t). \tag{A 7}$$

https://doi.org/10.1017/jfm.2020.153 Published online by Cambridge University Press

Using

$$\partial_t \boldsymbol{X} = \tau \hat{\boldsymbol{s}} + \nu \hat{\boldsymbol{n}}, \tag{A 8}$$

and (A 5),

$$\hat{\boldsymbol{s}} \cdot [(\boldsymbol{u}^{\pm}(\boldsymbol{x}, t) - \partial_t \boldsymbol{X}) \cdot \nabla \boldsymbol{u}^{\pm}(\boldsymbol{x}, t)]|_{\boldsymbol{x}=\boldsymbol{X}(\alpha,t)} = \left(\mu \mp \frac{\gamma}{2} - \tau\right) \left[\partial_s \left(\mu \mp \frac{\gamma}{2}\right) - \nu\kappa\right]. \tag{A 9}$$

The difference of the '+' and '−' terms on the right-hand side of (A 9) is

$$-(\mu - \tau)\partial_s \gamma - \gamma(\partial_s \mu - \nu\kappa). \tag{A 10}$$

The tangential component of the right-hand side of (A 6) is

$$-\partial_s [p]^{+}_{-}(\boldsymbol{x}, t)|_{\boldsymbol{x}=\boldsymbol{X}(\alpha,t)}. \tag{A 11}$$

Combining (A 7), (A 10) and (A 11), the tangential component of (A 6) is

$$\partial_t \gamma + (\mu - \tau)\partial_s \gamma + \gamma(\partial_s \mu - \nu\kappa) = \partial_s [p]^{+}_{-}, \tag{A 12}$$

or using α-derivatives,

$$\partial_\alpha s \partial_t \gamma + (\mu - \tau)\partial_\alpha \gamma + \gamma(\partial_\alpha \mu - \partial_\alpha s \nu\kappa) = \partial_\alpha [p]^{+}_{-}. \tag{A 13}$$

Appendix B. Numerical approximations

Vortex sheet computations can become expensive for long-time simulations. For a membrane in an oncoming flow (unidirectional and steady far upstream), the vortex wake is advected away from the membrane and it is possible to decrease resolution of the far-field wake (similarly to Alben (2009)) with only a small effect on the membrane and near-membrane wake dynamics.

We briefly describe the numerical approximations used to compute the wake dynamics in this work. For computational efficiency, we use a higher resolution near the membrane's trailing edge, and we prune the vortex wake in the far field. Once the free vortex sheet gets longer than one thousand points, we retain only the points of the free vortex sheet at local extrema of the circulation, to approximately maintain the zeroth and first moments of vorticity but using a small number of points. Because this portion of the sheet is far from the membrane, this approximation has a negligible effect on the dynamics. Examples are shown in figures 17 and 23, where the prescribed membrane parameters are $(R_1, R_3) = (10^{0.5}, 10^{1})$ and $(R_1, R_3) = (10^{0}, 10^{0.5})$, respectively.

We also use a point insertion/deletion scheme, but only sufficiently far from the membrane's trailing edge (e.g. implemented only more than 80 wake points from the trailing edge). As the free wake evolves, the distance between two consecutive points can increase beyond a given parameter d_1 (a fixed fraction of the wake smoothing parameter δ), and if this occurs, we insert new points using cubic interpolation to maintain wake resolution (Krasny 1987; Nitsche & Krasny 1994; Alben 2009). Similarly, at each time step, we check the distance between three consecutive points and if the distance between the first and third point is less than a specified threshold value d_2, then we delete the point in between the two to reduce the computational cost. During both processes, we always ensure that the total circulation is conserved for all times to satisfy Kelvin's circulation theorem.

https://doi.org/10.1017/jfm.2020.153 Published online by Cambridge University Press

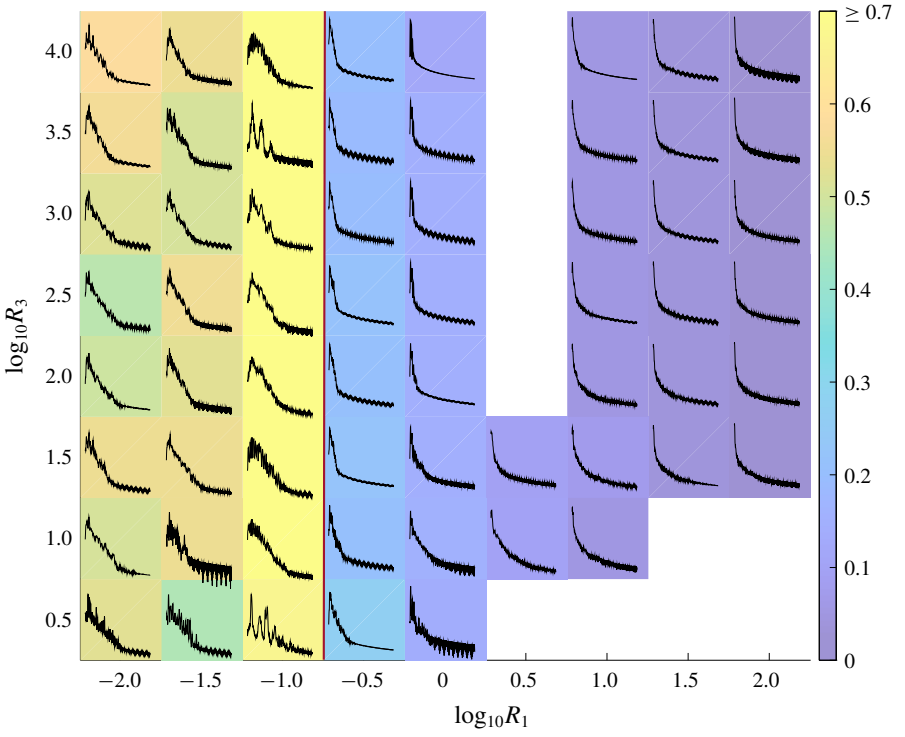


FIGURE 25. (Free–free) Surface plot of the mean frequency computed from the time series of the circulation, once the membranes have entered the large-amplitude regime with $T_0 = 10^{-2}$. The corresponding power spectra for each of the membranes are also shown on the surface plot. The data in the right-bottom corner are obtained for a shorter time and so we neglect the computational results for those values of R_1 and R_3.

Appendix C. Membrane frequencies in the free–free case

Since we have determined where in the parameter space the membrane is unstable, we can characterize the large-amplitude dynamics using the mean frequency and study how it depends on R_1 and R_3. We focus on the region where reliable frequency data can be obtained. As we have done previously, we compute the power spectrum from a plot of the circulation versus time, when the membrane has reached large-amplitude dynamics. In figure 25 we see that, in general, the frequency decreases with increasing R_1. For $R_1 = 10^{0.5}$ and R_3 ranging from 10^2 to 10^4, the membranes translate steadily (see figure 19) and the wake circulation tends to zero at large times. Therefore, the power spectra for those cases are zero and we omit them.

REFERENCES

ALBEN, S. 2008*a* Optimal flexibility of a flapping appendage in an inviscid fluid. *J. Fluid Mech.* **614**, 355–380.

ALBEN, S. 2008*b* The flapping-flag instability as a nonlinear eigenvalue problem. *Phys. Fluids* **20**, 104106.

https://doi.org/10.1017/jfm.2020.153 Published online by Cambridge University Press

ALBEN, S. 2009 Simulating the dynamics of flexible bodies and vortex sheets. *J. Comput. Phys.* **228** (7), 2587–2603.

ALBEN, S. 2010 Regularizing a vortex sheet near a separation point. *J. Comput. Phys.* **229** (13), 5280–5298.

ALBEN, S. 2012 The attraction between a flexible filament and a point vortex. *J. Fluid Mech.* **697**, 481–503.

ALBEN, S. 2015 Flag flutter in inviscid channel flow. *Phys. Fluids* **27** (3), 033603.

ALBEN, S. & SHELLEY, M. J. 2008 Flapping states of a flag in an inviscid fluid: bistability and the transition to chaos. *Phys. Rev. Lett.* **100** (7), 074301.

ARBÓS-TORRENT, S., GANAPATHISUBRAMANI, B. & PALACIOS, R. 2013 Leading- and trailing-edge effects on the aeromechanics of membrane aerofoils. *J. Fluids Struct.* **38**, 107–126.

ARGENTINA, M. & MAHADEVAN, L. 2005 Fluid-flow-induced flutter of a flag. *Proc. Natl Acad. Sci. USA* **102**, 1829–1834.

BATCHELOR, G. K. 1967 *An Introduction to Fluid Dynamics*. Cambridge University Press.

BRADY, M., LEONARD, A. & PULLIN, D. I. 1998 Regularized vortex sheet evolution in three dimensions. *J. Comput. Phys.* **146** (2), 520–545.

CARRIER, G. F. 1945 On the non-linear vibration problem of the elastic string. *Q. Appl. Maths* **3** (2), 157–165.

CARRIER, G. F. 1949 A note on the vibrating string. *Q. Appl. Maths* **7** (1), 97–101.

CHATTERJEE, P. & BRYANT, M. 2018 Aeroelastic-photovoltaic ribbons for integrated wind and solar energy harvesting. *Smart Mater. Struct.* **27** (8), 08LT01.

CHEN, M., JIA, L.-B., WU, Y.-F., YIN, X.-Z. & MA, Y.-B. 2014 Bifurcation and chaos of a flag in an inviscid flow. *J. Fluids Struct.* **45**, 124–137.

CHENEY, J. A., KONOW, N., BEARNOT, A. & SWARTZ, S. M. 2015 A wrinkle in flight: the role of elastin fibres in the mechanical behaviour of bat wing membranes. *J. R. Soc. Interface* **12** (106), 20141286.

CHORIN, A. J. & BERNARD, P. S. 1973 Discretization of a vortex sheet, with an example of roll-up. *J. Comput. Phys.* **13** (3), 423–429.

COLGATE, S. 1996 *Fundamentals of Sailing, Cruising, and Racing*. WW Norton and Company.

CONNELL, B. S. H. & YUE, D. K. P. 2007 Flapping dynamics of a flag in a uniform stream. *J. Fluid Mech.* **581**, 33–67.

DOARÉ, O. & MICHELIN, S. 2011 Piezoelectric coupling in energy-harvesting fluttering flexible plates: linear stability analysis and conversion efficiency. *J. Fluids Struct.* **27** (8), 1357–1375.

DRACHINSKY, A. & RAVEH, D. E. 2016 Limit-cycle oscillations of a pre-tensed membrane strip. *J. Fluids Struct.* **60**, 1–22.

ELLIS, P. D., WILLIAMS, J. E. & SHNEERSON, J. M. 1993 Surgical relief of snoring due to palatal flutter: a preliminary report. *Ann. R. Coll. Surg. Engrs* **75** (4), 286–290.

ELOY, C., LAGRANGE, R., SOUILLIEZ, C. & SCHOUVEILER, L. 2008 Aeroelastic instability of cantilevered flexible plates in uniform flow. *J. Fluid Mech.* **611**, 97–106.

ELOY, C., SOUILLIEZ, C. & SCHOUVEILER, L. 2007 Flutter of a rectangular plate. *J. Fluids Struct.* **23**, 904–919.

ERTURK, A., VIEIRA, W. G. R., DE MARQUI, C. JR & INMAN, D. J. 2010 On the energy harvesting potential of piezoaeroelastic systems. *Appl. Phys. Lett.* **96** (18), 184103.

FARLOW, S. J. 1993 *Partial Differential Equations for Scientists and Engineers*. Courier Corporation.

GHIAS, R., MITTAL, R. & DONG, H. 2007 A sharp interface immersed boundary method for compressible viscous flows. *J. Comput. Phys.* **225** (1), 528–553.

GIACOMELLO, A. & PORFIRI, M. 2011 Underwater energy harvesting from a heavy flag hosting ionic polymer metal composites. *J. Appl. Phys.* **109** (8), 084903.

GORDNIER, R. E. 2009 High fidelity computational simulation of a membrane wing airfoil. *J. Fluids Struct.* **25** (5), 897–917.

GRAFF, K. F. 1975 *Wave Motion in Elastic Solids*. Oxford University Press.

GRIFFITH, B. E., HORNUNG, R. D., MCQUEEN, D. M. & PESKIN, C. S. 2007 An adaptive, formally second order accurate version of the immersed boundary method. *J. Comput. Phys.* **223** (1), 10–49.

https://doi.org/10.1017/jfm.2020.153 Published online by Cambridge University Press

GRIFFITH, B. E. & PESKIN, C. S. 2005 On the order of accuracy of the immersed boundary method: higher order convergence rates for sufficiently smooth problems. *J. Comput. Phys.* **208** (1), 75–105.

HAMLET, C., SANTHANAKRISHNAN, A. & MILLER, L. A. 2011 A numerical study of the effects of bell pulsation dynamics and oral arms on the exchange currents generated by the upside-down jellyfish *Cassiopea xamachana*. *J. Expl Biol.* **214** (11), 1911–1921.

HARUO, K. 1975 Flutter of hanging roofs and curved membrane roofs. *Intl J. Solids Struct.* **11** (4), 477–492.

HOWELL, R. M., LUCEY, A. D., CARPENTER, P. W. & PITMAN, M. W. 2009 Interaction between a cantilevered-free flexible plate and ideal flow. *J. Fluids Struct.* **25** (3), 544–566.

HU, H., TAMAI, M. & MURPHY, J. T. 2008 Flexible-membrane airfoils at low Reynolds numbers. *J. Aircraft* **45** (5), 1767–1778.

HUANG, L. 1995*a* Flutter of cantilevered plates in axial flow. *J. Fluids Struct.* **9** (2), 127–147.

HUANG, L. 1995*b* Mechanical modeling of palatal snoring. *J. Acoust. Soc. Am.* **97** (6), 3642–3648.

HUANG, W. X. & SUNG, H. J. 2010 Three-dimensional simulation of a flapping flag in a uniform flow. *J. Fluid Mech.* **653**, 301–336.

JAWORSKI, J. W. & GORDNIER, R. E. 2012 High-order simulations of low Reynolds number membrane airfoils under prescribed motion. *J. Fluids Struct.* **31**, 49–66.

JONES, M. A. 2003 The separated flow of an inviscid fluid around a moving flat plate. *J. Fluid Mech.* **496**, 405–441.

JONES, M. A. & SHELLEY, M. J. 2005 Falling cards. *J. Fluid Mech.* **540**, 393–425.

KASHY, E., JOHNSON, D. A., MCINTYRE, J. & WOLFE, S. L. 1997 Transverse standing waves in a string with free ends. *Am. J. Phys.* **65** (4), 310–313.

KATZ, J. & PLOTKIN, A. 2001 *Low-speed Aerodynamics*, vol. 13. Cambridge University Press.

KIM, D., COSSÉ, J., CERDEIRA, C. H. & GHARIB, M. 2013 Flapping dynamics of an inverted flag. *J. Fluid Mech.* **736**, R1.

KIMBALL, J. 2009 *Physics of Sailing*. CRC Press.

KNUDSON, W. C. 1991 Recent advances in the field of long span tension structures. *Engng Struct.* **13** (2), 164–177.

KORNECKI, A., DOWELL, E. H. & O'BRIEN, J. 1976 On the aeroelastic instability of two-dimensional panels in uniform incompressible flow. *J. Sound Vib.* **47**, 163–178.

KRASNY, R. 1986 Desingularization of periodic vortex sheet roll-up. *J. Comput. Phys.* **65** (2), 292–313.

KRASNY, R. 1987 Computation of vortex sheet roll-up in the Trefftz plane. *J. Fluid Mech.* **184**, 123–155.

KRASNY, R. 1991 Vortex sheet computations: roll-up, wakes, separation. *Lectures Appl. Math.* **28** (1), 385–401.

LAUDER, G. V., MADDEN, P. G. A., MITTAL, R., DONG, H. & BOZKURTTAS, M. 2006 Locomotion with flexible propulsors: I. Experimental analysis of pectoral fin swimming in sunfish. *Bioinspir. Biomim.* **1** (4), S25.

LE MAÎTRE, O., HUBERSON, S. & DE CURSI, E. S. 1999 Unsteady model of sail and flow interaction. *J. Fluids Struct.* **13** (1), 37–59.

LIAN, Y. & SHYY, W. 2005 Numerical simulations of membrane wing aerodynamics for micro air vehicle applications. *J. Aircraft* **42** (4), 865–873.

LIAN, Y., SHYY, W., VIIERU, D. & ZHANG, B. 2003 Membrane wing aerodynamics for micro air vehicles. *Prog. Aerosp. Sci.* **39** (6–7), 425–465.

MANELA, A. & WEIDENFELD, M. 2017 The 'hanging flag' problem: on the heaving motion of a thin filament in the limit of small flexural stiffness. *J. Fluid Mech.* **829**, 190–213.

MICHELIN, S., SMITH, S. G. L. & GLOVER, B. J. 2008 Vortex shedding model of a flapping flag. *J. Fluid Mech.* **617**, 1–10.

NARASIMHA, R. 1968 Non-linear vibration of an elastic string. *J. Sound Vib.* **8** (1), 134–146.

NARDINI, M., ILLINGWORTH, S. J. & SANDBERG, R. D. 2018 Reduced-order modeling for fluid–structure interaction of membrane wings at low and moderate Reynolds numbers. In *2018 AIAA Aerospace Sciences Meeting,* 2018-1544. AIAA.

https://doi.org/10.1017/jfm.2020.153 Published online by Cambridge University Press

NAYFEH, A. H. & PAI, P. F. 2008 *Linear and Nonlinear Structural Mechanics*. John Wiley and Sons.

NEWMAN, B. G. 1987 Aerodynamic theory for membranes and sails. *Prog. Aerosp. Sci.* **24** (1), 1–27.

NEWMAN, B. G. & LOW, H. T. 1984 Two-dimensional impervious sails: experimental results compared with theory. *J. Fluid Mech.* **144**, 445–462.

NEWMAN, B. G. & PAIDOUSSIS, M. P. 1991 The stability of two-dimensional membranes in streaming flow. *J. Fluids Struct.* **5** (4), 443–454.

NITSCHE, M. & KRASNY, R. 1994 A numerical study of vortex ring formation at the edge of a circular tube. *J. Fluid Mech.* **276**, 139–161.

NITSCHE, M., TAYLOR, M. A. & KRASNY, R. 2003 Comparison of regularizations of vortex sheet motion. In *Computational Fluid and Solid Mechanics 2003*, pp. 1062–1065. Elsevier.

ORREGO, S., SHOELE, K., RUAS, A., DORAN, K., CAGGIANO, B., MITTAL, R. & KANG, S. H. 2017 Harvesting ambient wind energy with an inverted piezoelectric flag. *Appl. Energy* **194**, 212–222.

PESKIN, C. S. 2002 The immersed boundary method. *Acta Numerica* **11**, 479–517.

PIQUEE, J., LÓPEZ, I., BREITSAMTER, C., WÜCHNER, R. & BLETZINGER, K.-U. 2018 Aerodynamic characteristics of an elasto-flexible membrane wing based on experimental and numerical investigations. In *2018 Applied Aerodynamics Conference*, p. 3338.

PORFIRI, M. & PETERSON, S. D. 2013 Energy harvesting from fluids using ionic polymer metal composites. In *Advances in Energy Harvesting Methods*, pp. 221–239. Springer.

PULLIN, D. I. & WANG, Z. J. 2004 Unsteady forces on an accelerating plate and application to hovering insect flight. *J. Fluid Mech.* **509**, 1–21.

ROJRATSIRIKUL, P., WANG, Z. & GURSUL, I. 2009 Unsteady fluid–structure interactions of membrane airfoils at low Reynolds numbers. *Exp. Fluids* **46** (5), 859–872.

ROMA, A. M., PESKIN, C. S. & BERGER, M. J. 1999 An adaptive version of the immersed boundary method. *J. Comput. Phys.* **153** (2), 509–534.

SAFFMAN, P. G. 1992 *Vortex Dynamics*. Cambridge University Press.

SCHOMBERG, T., GERLAND, F., LIESE, F., WÜNSCH, O. & RUETTEN, M. 2018 Transition manipulation by the use of an electrorheologically driven membrane. In *2018 Flow Control Conference*, p. 3213.

SHELLEY, M. J., VANDENBERGHE, N. & ZHANG, J. 2005 Heavy flags undergo spontaneous oscillations in flowing water. *Phys. Rev. Lett.* **94** (9), 094302.

SHELLEY, M. J. & ZHANG, J. 2011 Flapping and bending bodies interacting with fluid flows. *Annu. Rev. Fluid Mech.* **43**, 449–465.

SHENG, J. X., YSASI, A., KOLOMENSKIY, D., KANSO, E., NITSCHE, M. & SCHNEIDER, K. 2012 Simulating vortex wakes of flapping plates. In *Natural Locomotion in Fluids and on Surfaces*, pp. 255–262. Springer.

SHUKLA, R. K. & ELDREDGE, J. D. 2007 An inviscid model for vortex shedding from a deforming body. *Theor. Comput. Fluid Dyn.* **21** (5), 343–368.

SONG, A., TIAN, X., ISRAELI, E., GALVAO, R., BISHOP, K., SWARTZ, S. & BREUER, K. 2008 Aeromechanics of membrane wings with implications for animal flight. *AIAA J.* **46** (8), 2096–2106.

STANFORD, B., IFJU, P., ALBERTANI, R. & SHYY, W. 2008 Fixed membrane wings for micro air vehicles: experimental characterization, numerical modeling, and tailoring. *Prog. Aerosp. Sci.* **44** (4), 258–294.

SUNNY, M. R., SULTAN, C. & KAPANIA, R. K. 2014 Optimal energy harvesting from a membrane attached to a tensegrity structure. *AIAA J.* **52** (2), 307–319.

SYGULSKI, R. 1996 Dynamic stability of pneumatic structures in wind: theory and experiment. *J. Fluids Struct.* **10** (8), 945–963.

SYGULSKI, R. 1997 Numerical analysis of membrane stability in air flow. *J. Sound Vib.* **201** (3), 281–292.

SYGULSKI, R. 2007 Stability of membrane in low subsonic flow. *Intl J. Non-Linear Mech.* **42** (1), 196–202.

https://doi.org/10.1017/jfm.2020.153 Published online by Cambridge University Press

TADJBAKHSH, I. 1966 The variational theory of the plane motion of the extensible elastica. *Intl J. Engng Sci.* **4** (4), 433–450.

TAIRA, K. & COLONIUS, T. 2007 The immersed boundary method: a projection approach. *J. Comput. Phys.* **225** (2), 2118–2137.

TAMAI, M., MURPHY, J. & HU, H. 2008 An experimental study of flexible membrane airfoils at low Reynolds numbers. In *46th AIAA Aerospace Sciences Meeting and Exhibit*, p. 580.

TANEDA, S. 1968 Waving motions of flags. *J. Phys. Soc. Japan* **24**, 392–401.

TANG, D. M., YAMAMOTO, H. & DOWELL, E. H. 2003 Flutter and limit cycle oscillations of two-dimensional panels in three-dimensional axial flow. *J. Fluids Struct.* **17** (2), 225–242.

TIAN, F.-B., LUO, H., ZHU, L., LIAO, J. C. & LU, X.-Y. 2011 An efficient immersed boundary-lattice Boltzmann method for the hydrodynamic interaction of elastic filaments. *J. Comput. Phys.* **230** (19), 7266–7283.

TIMPE, A., ZHANG, Z., HUBNER, J. & UKEILEY, L. 2013 Passive flow control by membrane wings for aerodynamic benefit. *Exp. Fluids* **54** (3), 1471.

TIOMKIN, S. & RAVEH, D. E. 2017 On the stability of two-dimensional membrane wings. *J. Fluids Struct.* **71**, 143–163.

TRIANTAFYLLOU, M. S. & HOWELL, C. T. 1994 Dynamic response of cables under negative tension: an ill-posed problem. *J. Sound Vib.* **173** (4), 433–447.

TYTELL, E. D., HSU, C.-Y., WILLIAMS, T. L., COHEN, A. H. & FAUCI, L. J. 2010 Interactions between internal forces, body stiffness, and fluid environment in a neuromechanical model of lamprey swimming. *Proc. Natl Acad. Sci. USA* **107** (46), 19832–19837.

TZEZANA, G. A. & BREUER, K. S. 2019 Thrust, drag and wake structure in flapping compliant membrane wings. *J. Fluid Mech.* **862**, 871–888.

WALDMAN, R. M. & BREUER, K. S. 2013 Shape, lift, and vibrations of highly compliant membrane wings. In *43rd AIAA Fluid Dynamics Conference*, p. 3177.

WALDMAN, R. M. & BREUER, K. S. 2017 Camber and aerodynamic performance of compliant membrane wings. *J. Fluids Struct.* **68**, 390–402.

WANG, X., ALBEN, S., LI, C. & YOUNG, Y. L. 2016 Stability and scalability of piezoelectric flags. *Phys. Fluids* **28** (2), 023601.

WANG, Z., REBEIZ, E. E. & SHAPSHAY, S. M. 2002 Laser soft palate 'stiffening': an alternative to uvulopalatopharyngoplasty. *Lasers in Surgery and Medicine: The Official Journal of the American Society for Laser Medicine and Surgery* **30** (1), 40–43.

WATANABE, Y., SUZUKI, S., SUGIHARA, M. & SUEOKA, Y. 2002 An experimental study of paper flutter. *J. Fluids Struct.* **16** (4), 529–542.

WELCH, P. D. 1967 The use of fast fourier transform for the estimation of power spectra: a method based on time averaging over short, modified periodograms. *IEEE Trans. Audio Electroacoust.* **15** (2), 70–73.

WILLIAMSON, C. H. K. & ROSHKO, A. 1988 Vortex formation in the wake of an oscillating cylinder. *J. Fluids Struct.* **2** (4), 355–381.

XU, L., NITSCHE, M. & KRASNY, R. 2017 Computation of the starting vortex flow past a flat plate. *Proc. IUTAM* **20**, 136–143.

YANG, S. & SULTAN, C. 2016 Modeling of tensegrity-membrane systems. *Intl J. Solids Struct.* **82**, 125–143.

ZHANG, J., CHILDRESS, S., LIBCHABER, A. & SHELLEY, M. J. 2000 Flexible filaments in a flowing soap film as a model for flags in a two dimensional wind. *Nature* **408**, 835–839.

ZHU, L. & PESKIN, C. S. 2002 Simulation of a flapping flexible filament in a flowing soap film by the immersed boundary method. *J. Comput. Phys.* **179**, 452–468.

https://doi.org/10.1017/jfm.2020.153 Published online by Cambridge University Press